



# A microstructure-sensitive analytical solution for short fatigue crack growth rate in metallic materials

Daniel J. Long<sup>\*</sup>, Yang Liu, Weifeng Wan, Fionn P.E. Dunne

Department of Materials, Royal School of Mines, Imperial College London, SW7 2AZ, UK

## ABSTRACT

Short fatigue crack growth in engineering alloys is among the most prominent challenges in mechanics of materials. Owing to its microstructural sensitivity, advanced and computationally expensive numerical methods are required to solve for crack growth rate. A novel mechanistic analytical model is presented, which adopts a stored energy density fracture criterion. Full-field implementation of the model in polycrystalline materials is achieved using a crystallographic crack-path prediction method based on a local stress intensity factor term. The model is applied to a range of Zircaloy-4 microstructures and demonstrates strong agreement with experimental rates and crack paths. Growth rate fluctuations across individual grains and substantial texture sensitivity are captured using the model. More broadly, this work demonstrates the benefits of mechanistic analytical modelling over conventional fracture mechanics and recent numerical approaches for accurate material performance predictions and design. Additionally, it offers a significant computer processing time reduction compared with state-of-the-art numerical methods.

## 1. Introduction

The intricacy of the short fatigue crack growth (FCG) problem has meant that growth rates are not easily predicted, leaving a knowledge gap which can only be addressed through mechanistic understanding. This paper presents a deterministic analytical solution to overcome this obstacle. Since the beginning of the industrial revolution, conventional fracture mechanics methods for FCG have enabled the progressive improvement of engineering design through failure mechanism understanding [1]. For example, Paris' Law [2], which relates crack propagation rate to stress intensity factor (SIF) has been widely used to characterise the stage II FCG behaviour of metallic materials. However, for modern and future industrial applications (e.g., nuclear reactor fuel cladding [3], pressure vessels [4], aerospace turbine components [5,6], submarine power cables [7]), it is recognised that component lifetimes are dominated by stage I, viz., crack nucleation and short FCG, as illustrated in Fig. 1. Hence, since the length-scales for these processes are generally of the same order as microstructural features, and of the crack tip plastic zone size, microstructure variations and plasticity become crucial. Consequently, classical approaches are made redundant, and the necessity for new microstructure-sensitive fracture mechanics becomes clear.

In this paper, microstructurally short fatigue cracks follow the definition adopted by McDowell [11], in which the length of the crack is of the same order as several microstructure features. In addition, only physically short cracks are considered, i.e., where crack length is less

than 1 mm. Microstructural features such as grain boundaries add further complexity to short FCG modelling as they can strongly influence the local behaviour in terms of rate and path due to impedance of dislocation motion, pileup of dislocations, and stress localisation. For example, Wen et al. [12] quantified the resistance of grain boundaries (in terms of a change in FCG rate) as a function of tilt and twist angles between crack planes in an Al-Cu alloy. Results indicated that growth rate retardation was strongly linked with twist angle across boundaries, as there was a strong positive correlation. The authors also indicated that the distance over which microstructure features can affect rates of FCG is between 5 – 20  $\mu\text{m}$ . Hence, for many engineering materials with grain sizes of this magnitude, grain boundary effects can be important to consider. These findings agree with earlier experimental work by Zhai et al. [13]. Atomistic modelling by Sangid et al. [14] was used to investigate the behaviour of a range of grain boundary types in terms of the energy barriers for and hence resistance against dislocation transmission. Trends were compared with in-situ transmission electron microscopy (TEM) data at grain boundaries, showing strong agreement. However, approaches such as this demand significant computer processing capabilities. Chowdhury et al. [15] used a similar approach in modelling the FCG resistance of other microstructural obstacles such as nanoscale twin boundaries. Atomistic modelling was used to generate energy barrier data, which was used as an input to a dislocation mechanics based FCG model; the methodology addresses key aspects of microstructure sensitive crack growth including slip irreversibility and the threshold SIF range but lacks direct validation against experimental data. Furthermore, the approach is inefficient as it relies on atomistic

<sup>\*</sup> Corresponding author.

E-mail address: [d.long20@imperial.ac.uk](mailto:d.long20@imperial.ac.uk) (D.J. Long).

**Nomenclature**

$a$	Crack length	$M$	Total number of slip systems
$a_e$	Effective crack length	$n$	Number of dislocations per cycle
$b$	Burgers vector magnitude	$P$	Applied load
$B$	Beam depth	$r_{avg}$	Mean crack tip to dislocation distance
$da/dN$	Crack growth rate	$R$	Cyclic loading ratio
$dG/dN$	Cyclic stored energy density	$S$	Distance between support pins
$d\gamma^P$	Plastic shear strain increment	$W$	Beam height
$G$	Stored energy density	$\gamma^e$	Elastic shear strain
$G_c$	Critical stored energy density	$\gamma^P$	Plastic shear strain
$G_r$	Residual stored energy density	$\Delta a$	Crack length increment
$i$	Slip system number	$\Delta K_{\theta}$	Cyclic shear stress intensity factor
$j$	Selected slip system for crack path	$\Delta K^{\infty}$	Cyclic applied stress intensity factor
$K_I$	Mode I stress intensity factor	$\theta$	Crack growth direction-slip trace angle
$K_{II}$	Mode II stress intensity factor	$\mu$	Shear modulus
$K_{\theta}$	In-plane shear stress intensity factor	$\nu$	Poisson's ratio
$K_{\theta}^{\perp}$	In-plane dislocation shielding factor	$\xi$	Fraction of plastic strain energy stored
$l$	Mean dislocation spacing	$\rho_{GND}$	Density of GNDs
$l_s$	Dislocation line length	$\rho_{SSD}$	Density of SSDs
		$\tau_c$	Critical resolved shear stress
		$\chi$	Residual energy fraction after cracking

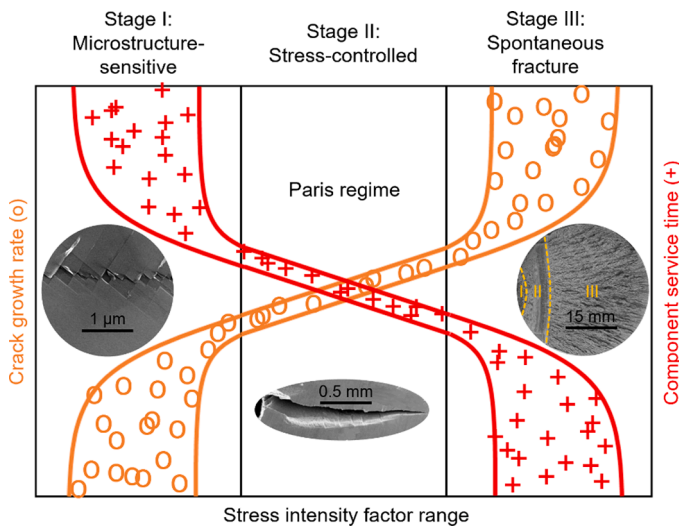


**Fig. 1.** Illustration showing evolution of FCG rate trends with increasing SIF range from stage I (short cracks) to stage III (unstable growth). The corresponding and inversely proportional component service time trend is also shown, demonstrating that component lifetimes are dominated by stage I cracking. Stage II, denoted the 'Paris regime', is clearly strongly linked with SIF, and hence, is easily characterised. Conversely, stage I suffers from data scatter (when applying classical fracture mechanics) due to microstructure sensitivity. A stage I micrograph [8] also demonstrates microstructure sensitivity of crack path (which is clearly linked with crystallography), while stage II paths [9] are typically orthogonal to the remote applied stress. The stage III figure of a fracture surface is from Milan et al. [10].

modelling for specific microstructure interactions. Chowdhury et al. [16,17] also presented detailed mechanistic models for short FCG in nano-twinned materials based on twin-slip interactions, slip irreversibility and the Peierls-Nabarro model. A continuum model for FCG was developed based on the threshold SIF range; results compared favourably with a range of experimental data, but the model could not be applied to explicitly predict rates of growth in real materials.

To capture microscale material behaviour, crystal plasticity finite element (CPFE) modelling is a potential candidate. This approach was used in combination with the eXtended Finite Element Method (XFEM)

by Zhang et al. [18] to simulate short FCG in a nickel-based superalloy. Crack path phenomena such as tortuosity were predicted using a maximum slip criterion, albeit using representative modelling, rather than direct simulation of experiments. Growth rate trends were reasonably captured, though not precisely, using critical cumulative shear strain. An arbitrary scaling factor was required to 'fit' simulated rates to experiment, demonstrating a lack of mechanistic understanding. XFEM enables simulation of crack paths in any direction without a priori specification, while minimising computational cost, since remeshing is not required. However, practically, linking the CPFE-XFEM approach with the component scale remains inaccessible due to the associated increase in processing requirements [19]. Recent modelling work by Shen et al. [20] aimed to bridge microstructural and component length-scales for crack nucleation in  $\alpha/\beta$  Ti-64 microstructures; fatigue life predictions were found to be consistent with experimental data. However, an obvious drawback of the approach is that it requires extensive fitting and calibration for each material. Cohesive zones modelling linked with CPFE has been widely used [21–23] to predict microscale cracking but comes with the drawback of crack path confinement by mesh geometry.

Modern numerical methods used to predict short FCG are enormously computationally expensive. A key factor responsible for the computational cost of XFEM is that the governing equations which solve for crack tip displacements are in differential form [24]. Bond-based peridynamics modelling of FCG offers a more rapid alternative to this, since it is formulated using spatial integrals. The method was first introduced by Silling [25], and has been successfully implemented to simulate FCG in numerous materials [26–28]. However, the approach accounts only for linear elasticity, and requires coupling with e.g., CPFE models, to capture the microscale plasticity associated with short FCG. Crystal plasticity code within phase field modelling (PFM) has also been used to capture micromechanical material behaviour [29,30]. Ai et al. [30] presented a multi-physics PFM approach to predict crack nucleation and short FCG in battery electrode particles. Experimental observations including nucleation sites were captured, but not growth rate, and the scale of the model was not sufficiently large to predict realistic material performance. High fidelity PFM approaches, which are underpinned by mechanistic understanding, are inherently computationally expensive, as they require complex numerical integration schemes [31]. In summary, high fidelity analytical models, such as the one presented in this paper offer minimised computational expense compared with state-of-the-art numerical methods, all while remaining

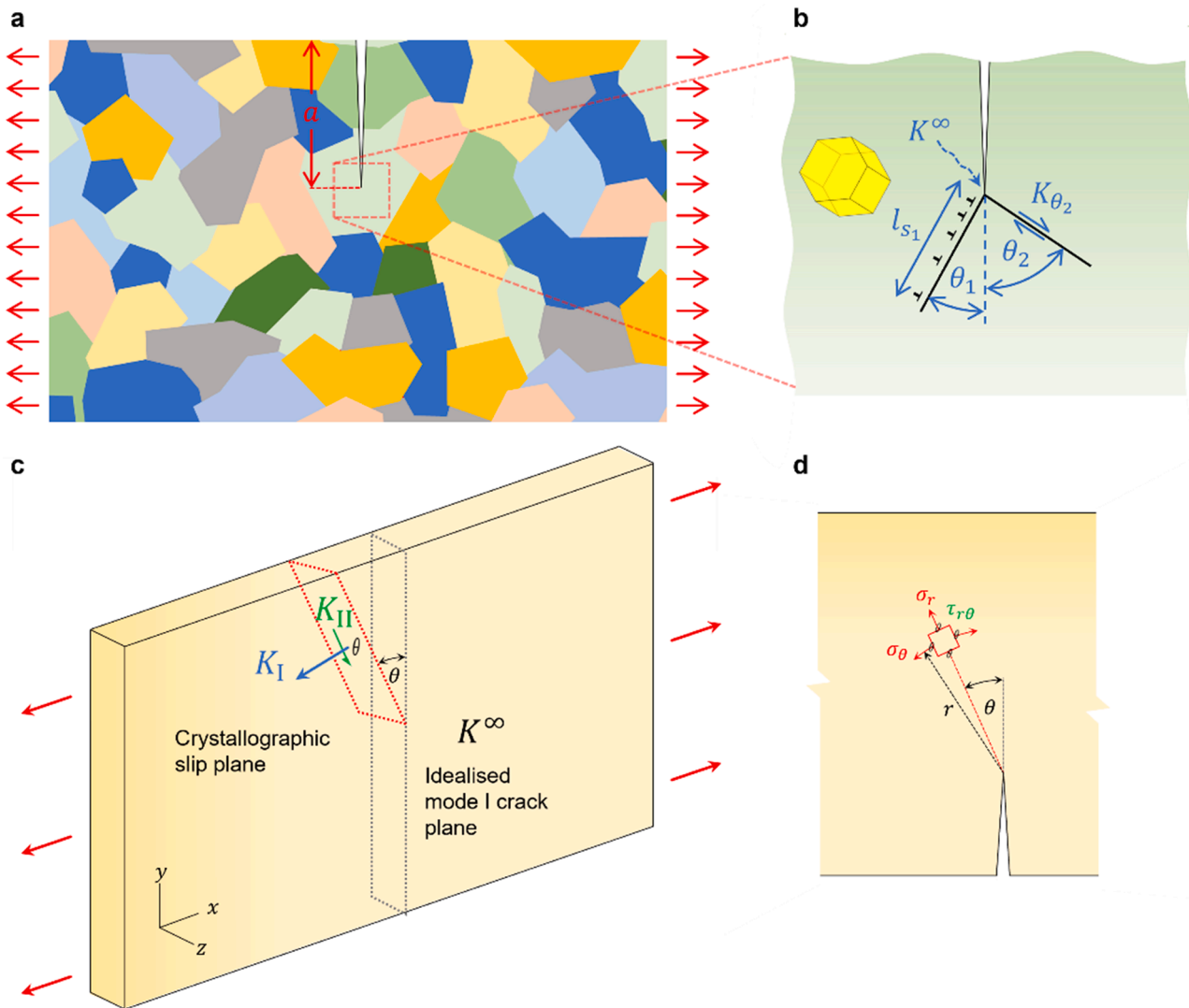


**Fig. 2.** Overview of analytical modelling formulation within a polycrystal. a. Illustration of a microstructurally short crack within a polycrystal. b. Corresponding representation of crack tip within a single grain with sample slip line directions defined by  $\theta_1$  and  $\theta_2$ . c. Illustration of mode I and II SIFs acting on a crystallographic slip plane with  $x$ ,  $y$ , and  $z$  components. d. Polar stress around the crack tip, adapted from Gdoutos [42].

deterministic. Evidently, numerical methods have the potential to offer reliable solutions to the short FCG problem but are stifled by a lack of physical understanding and computer processing limitations. Recently, several articles have been published by Zhou et al. [32–34] proposing a generalised multi-scale methodology for prediction of fatigue lives and performance of a range of steels with and without hierarchical microstructures. Using the crack tip sliding displacement range ( $\Delta$ CTS $D$ ) as the driving force for crack growth, analytical models were used in combination with finite element modelling, incorporating important aspects of microstructure (e.g., grain size, morphology, local elastic properties) with high computational efficiency. The approach could capture microstructure-linked differences in fatigue life across a range of applied stresses. Similar work by Ito et al. [35] presented a model which could capture the influence of grain boundaries on the FCG driving force. However, the models have not been applied to explicitly predict aspects of microstructurally short FCG (i.e., path or rate), which is a key aim of the current work. In this paper, a novel mechanistic analytical model is presented, adopting a stored energy density (SED) fracture criterion, and a new crystallographic crack path prediction method, based on a local SIF (for full-field implementation). Experimental FCG rates and paths in Zircaloy-4 samples are used as a case study for comparison. To capture the ‘starting’ FCG behaviour, a dislocation shielding

model is also incorporated. Compared with classical elastic FCG driving forces, e.g., Griffith energy [36], SED offers much greater microstructure-sensitivity [37]. Furthermore, SED is non-singular at the crack tip [38], compared with stress and strain, which are singular [39]. SED is a measure of energy stored in inter-connected dislocation structure, i.e., lattice curvature, ahead of a crack tip for example. The cyclic accumulation of this elastically recoverable energy is argued in this paper to be the driving force for short FCG. Hence, when the energy ahead of a crack tip exceeds a critical value (sufficient to open a crack), crack growth will occur. It has been shown in previous work to be a key mechanistic driver for fatigue crack nucleation and growth [40].

## 2. Model development and implementation

### 2.1. Development of an analytical model for cyclic stored energy density at a crack tip

The FCG rate model is developed here based on a SED fracture criterion, for which a critical value,  $G_c$ , is required to allow crack extension. The crack tip SED must therefore be calculated before determining growth rate. Xu et al. [38] derived a one dimensional (single slip line contribution) analytical solution for crack tip SED based on the

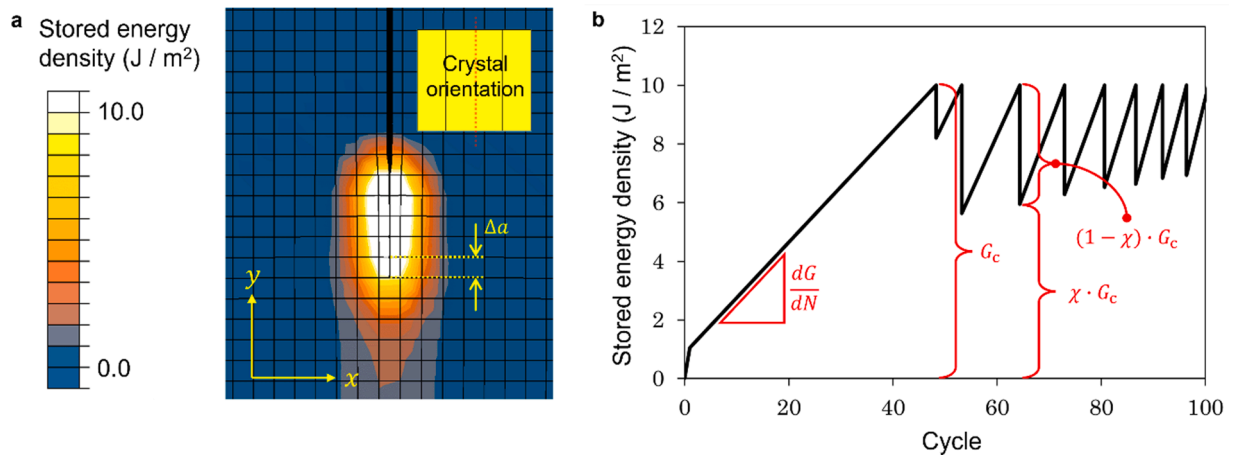


**Fig. 3.** Mechanistic understanding of single crystal crack propagation from CPFE simulation. a. CPFE-simulated SED field about a growing crack within a single crystal. The orientation selected for this enables crack growth perpendicular to the primary loading direction (x-direction). As shown, the crack path is straight and vertical, and propagates along prismatic slip planes perpendicular to their Burgers vector directions. The crack increment length,  $\Delta a$  is shown also, and is equal to the mesh size, 10  $\mu\text{m}$ . The critical SED is arbitrarily selected to be 10  $\text{J}/\text{m}^2$ . b. Evolution of SED ahead of the growing crack tip with increasing cycle number, i.e., after the crack propagates, a new crack tip is defined. Concepts of cyclic SED,  $dG/dN$  and residual stored energy density fraction,  $\chi$ , are introduced.

accumulation of geometrically necessary dislocations (GNDs) due to strong local lattice curvature. The expression was derived by integrating over shear plastic strain increments along a given slip line, as  $G =$

$$\int_0^{l_s} \frac{\tau dy^p}{\sqrt{\rho_{\text{GND}}}}, \text{ where } \tau \text{ is shear stress, } dy^p \text{ is plastic shear strain increment,}$$

$\rho_{\text{GND}}$  is density of GNDs, and  $l_s$  is the total slip line length, i.e., integration of SED is considered between the crack tip and the edge of the plastic zone. Note that in the current paper, SED is written in terms of local microstructural quantities, rather than the conventional mean-field approach [40], as described by Xu et al. [38]. When integrated, the expression gives a non-singular solution for crack tip SED, which is linked with classical fracture mechanics through SIF as  $G =$

$\left[ \frac{4\tau_c b(1-2\nu)}{\pi\mu} \right]^{\frac{1}{2}} \cdot K_{\theta}$ .  $K_{\theta}$  is a shear component of the remote mode I crack tip SIF (which is a function of remote loading and projected crack length,  $a$  only), acting on their respective slip systems. However, the key shortcomings of this formulation are (i) that it accounts for single slip only at the crack tip (assuming that a single slip system contributes to crack tip SED), and (ii) its failure to capture the influence of mode II shear on  $K_{\theta}$ . To address (i), multiple slip system contributions are accounted for by summation. In addition, the fraction of total energy stored in dislocation structure [41],  $\xi$ , is incorporated as follows from Xu et al. [38].

$$G = \xi \sum_{i=1}^M \left[ \frac{4\tau_c^i b^i (1-2\nu)}{\pi\mu} \right]^{\frac{1}{2}} \cdot K_{\theta}^i \quad (1)$$

where  $i$  is slip system number,  $\tau_c$  is critical resolved shear stress (CRSS) of the slip system,  $b$  is Burgers vector magnitude,  $\nu$  and  $\mu$  are Poisson's ratio and shear modulus, respectively, and  $\Delta K_{\theta}$  is an orientation-specific shear SIF, linked with remote SIF by  $\Delta K_{\theta} = \frac{1}{4} \left( \sin\left(\frac{\theta}{2}\right) + \sin\left(\frac{3\theta}{2}\right) \right) \cdot \Delta K^{\infty}$  (see Fig. 2).  $M$  is the total number of active slip systems. The localisation of slip, and hence dislocations at the crack tip is represented schematically in Fig. 2a and b. Based the 3D orientation of individual slip planes with respect to the remote loading direction (see Fig. 2c), a mode I local SIF,  $K_I$  may be estimated by calculating the component of remote SIF acting along slip plane normal via a simple Mohr's circle analysis. Similarly, the mode II component,  $K_{II}$  is assumed equivalent to the in-plane shear component of remote SIF. This is described in Fig. 2c.

By energy conservation and classical fracture mechanics, it follows that Eq. (1) is subject to the constraint  $\sqrt{\sum_{i=1}^M K_{\theta}^i{}^2} \leq K^{\infty}$ , since  $K^{\infty 2} \propto G$  [1]. This root-mean-square formulation links the local crystallographic

SIF terms with the remote applied SIF. Unlike CPFE modelling, the current method does not capture explicit levels of slip, and hence, the local stress state is not updated directly as dislocation slip activity occurs. Therefore, the constraint is an approximation which is essential for ensuring that the SED contributions of  $M$  slip systems are not over-predicted, and are relevant to the applied SIF, i.e., increasing the number of slip systems does not necessarily increase slip activity beyond a certain point. In cases where the constraint is not met, Eq. (1) is rewritten as,

$$G = \xi \left( \frac{K^{\infty}}{\sqrt{\sum_{i=1}^M K_{\theta}^i{}^2}} \right) \sum_{i=1}^M \left[ \frac{4\tau_c^i b^i (1-2\nu)}{\pi\mu} \right]^{\frac{1}{2}} \cdot K_{\theta}^i \quad (2)$$

Since the CRSS of the 2nd order  $\langle c+a \rangle$  slip system is significantly larger than the other Zircaloy-4 slip systems, it is assumed that all crack tip deformation is accommodated by basal, prismatic, and 1st order pyramidal slip systems, i.e.,  $M = 24$ . This constraint is also necessary to ensure SED is not over-estimated. To address (ii), the shear SIF term is modified to account for mode II contributions. Previously, it was assumed that only the remote mode I load contributed to shear along the slip line; hence, for a slip plane whose x-y trace lay parallel with the y-axis, there would be no shear SIF, and hence no SED. Here, the mode II contribution is incorporated by adding its effect to the polar shear stress,  $\tau_{r\theta}$  (see Fig. 7c and d). Assuming no slip step due to the presence of a dislocation free zone (DFZ) ahead of the crack tip, the plastic shear strain along a slip line is given by  $\gamma^p = -\gamma^c = -\frac{\tau_{r\theta}}{\mu}$ . For mode I SIF on the slip plane, the polar shear stress contribution is given by  $\tau_{r\theta, I} = \frac{K_I}{\sqrt{2\pi r}} \left( \frac{1}{4} \sin\left(\frac{\theta}{2}\right) + \frac{1}{4} \sin\left(\frac{3\theta}{2}\right) \right)$  [42]. For mode II, the contribution is  $\tau_{r\theta, II} = \frac{K_{II}}{\sqrt{2\pi r}} \left( \frac{1}{4} \cos\left(\frac{\theta}{2}\right) + \frac{3}{4} \cos\left(\frac{3\theta}{2}\right) \right)$  [42]. Writing the shear stress,  $\tau_{r\theta}$  in terms of  $K_{\theta}$  gives  $\tau_{r\theta} = \frac{K_{\theta}}{\sqrt{2\pi r}} = \tau_{r\theta, I} + \tau_{r\theta, II}$ . Hence, the modified shear SIF, accounting for modes I and II on the  $i$ th slip plane is given by,

$$K_{\theta}^i = \frac{1}{4} \left[ \left( \sin\left(\frac{\theta}{2}\right) + \sin\left(\frac{3\theta}{2}\right) \right) \cdot K_I^i + \left( \cos\left(\frac{\theta}{2}\right) + 3\cos\left(\frac{3\theta}{2}\right) \right) \cdot K_{II}^i \right] \quad (3)$$

The purpose of the current model is not to capture the precise crack tip stress-state or slip levels, but rather to capture, more generally, the influence of crystallography (discrete slip system orientation, elastic anisotropy, etc.) on the short FCG driving force (argued here to be SED), and hence growth rate. The evolution of SED with fatigue cycles or cyclic SED is approximated in this work for loading ratios of  $R \geq 0$  to avoid complications associated with fully reversed loading, including crack tip

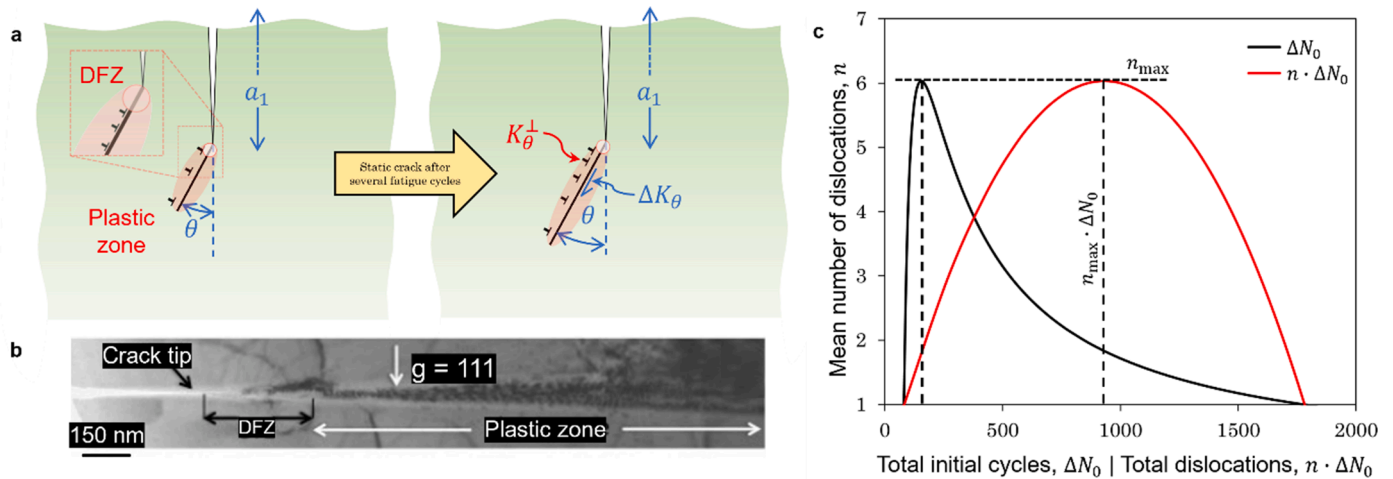


**Fig. 4.** Depiction of dislocation shielding model with mean emitted crack tip dislocations strategy. a. Schematic representation of cyclic dislocation shielding mechanism. After several fatigue cycles, dislocations accumulate ahead of the static crack tip, affecting the local shear SIF. The comparatively small DFZ is also shown. b. TEM image showing crack tip dislocations and DFZ in a nickel-based super alloy [45,49]. This indicates that for a physically and microstructurally short tensile crack, the DFZ is of the order of  $0.5 \mu\text{m}$ . c. Sample dislocation number calculation showing relationship with initial number of cycles and total number of dislocations before crack extension. Maximum number of dislocations is selected such that dislocation shielding is maximised for the initial crack length, as shown.

back-stresses, crack closure, etc.); hence, the static value for SIF in the static SED expression (Eq. (2)) is replaced by SIF range. Cyclic SED is then written as  $\frac{dG}{dN} = \xi \sum_{i=1}^M \left[ \frac{4\tau_c^i b^i (1-2\nu)}{\pi\mu} \right]^{\frac{1}{2}} \cdot \Delta K_\theta^i$ .

## 2.2. Analytical solution for crack growth rate

To illustrate the behaviour of SED at a crack tip, a simple single crystal CPFEM-XFEM simulation is performed. Figure 3a shows the predicted crack tip SED field for the single crystal orientation shown. Figure 3b shows the crack tip SED evolution during  $R = 0$  fatigue loading.

The cyclic SED,  $\frac{dG}{dN}$  is shown to increase with cycle number. For small numbers of cycles, SED increases approximately linearly until the critical value is reached. At this point, the crack extends by some increment,  $\Delta a$  (Fig. 3a). This gives a SED discontinuity as a new crack tip is created. However, it is clear (for the current  $\Delta a$ ) that crack tip SED remains greater than zero after extension. Hence, there is residual SED,  $G_r$ , which is shown to vary with crack length.  $G_r$  is characterised here as a fraction of the critical value by  $\chi = \frac{G_r}{G_c}$ . The FCG rate may be written in terms of crack length increment as  $\frac{da}{dN} = \frac{\Delta a}{\Delta N}$ , where  $\Delta N$  is the number of cycles required to reach  $G_c$ . For stable FCG, the cumulative SED required to achieve this is  $\Delta G = (1 - \chi) \cdot G_c$ . For small numbers of cycles (small  $\Delta N$ ), cyclic SED is expressed as  $\frac{dG}{dN} = \frac{\Delta G}{\Delta N}$ . Therefore,  $\Delta N = \frac{\Delta G}{dG/dN}$ . FCG rate is thereby expressed as,

$$\frac{da}{dN} = \frac{\Delta a}{(1 - \chi) \cdot G_c} \cdot \frac{dG}{dN} \quad (4)$$

where  $\Delta a$  is an arbitrarily selected crack extension increment, and  $\chi$  is dependent upon  $\Delta a$ .  $\frac{dG}{dN}$  varies depending on loading conditions, crack length, and material. Incorporation of the expression for cyclic SED gives,

$$\frac{da}{dN} = \frac{\Delta a}{(1 - \chi) \cdot G_c} \cdot \xi \sum_{i=1}^M \left[ \frac{4\tau_c^i b^i (1 - 2\nu)}{\pi\mu} \right]^{\frac{1}{2}} \cdot \Delta K_\theta^i \quad (5)$$

A drawback of the model in this form is that for some arbitrary  $\Delta a$ , the residual SED fraction,  $\chi$ , is unknown. Since SED accumulates under plastic deformation, it may be assumed that residual SED equals zero at the plastic zone edge, such that  $\Delta a = l_s$  (slip line length), i.e., where  $\Delta a = l_s$ ,  $G_r = \chi = 0$ . Hence, the evolution of residual SED with increasing

crack length can effectively be captured using slip line length evolution. An expression for slip line length can be derived from fracture mechanics methods for estimating plastic zone radius [43] as  $l_s = \frac{(1-2\nu)}{2\pi} \left( \frac{K_\theta}{\tau_c} \right)^2$  [38]. Hence, crack length increment,  $\Delta a$ , is given mechanistic basis, and the residual SED term,  $\chi$ , can be reduced to zero at the end of the slip line. The value of  $l_s$  will depend on crack direction, which is confined to the set of  $M$  slip systems, where the selected slip system for crack path is  $i = j$ , i.e.,  $j$  represents the slip system index number which controls crack propagation direction. Since the crack length considered for remote SIF calculation is projected length, the crack length increment is now written in terms of crack direction and slip line length as  $\Delta a = l_s \cos(\theta)$  (see Fig. 2 for details). FCG rate is now therefore dependent on crack propagation direction and is given by,

$$\frac{da}{dN} = \frac{l_s \cos\theta}{G_c} \cdot \xi \sum_{i=1}^M \left[ \frac{4\tau_c^i b^i (1 - 2\nu)}{\pi\mu} \right]^{\frac{1}{2}} \cdot \Delta K_\theta^i \quad (6)$$

## 2.3. Incorporation of a dislocation shielding parameter

For predicting microstructure sensitive FCG rate, it is useful to link microstructural parameters with classical fracture mechanics approaches, i.e., via SIF. However, crack tip SIF alone describes only the elastic behaviour of the material, and therefore does not account for the effects of cyclic plasticity on the local stress field. Due to the vast number of cycles often required to propagate short or stage I fatigue cracks, this is an important consideration. At the microstructural level, this effect is referred to as dislocation shielding [44,45], as individual dislocations contribute towards the diminution of stress. Experimental observations of dislocation emission from crack tips using TEM show that shielding dislocations, which make up the plastic zone, first cross the DFZ [45,46]; this is consistent with the theory of the current analytical model. While it may seem that dislocations have no shielding effect at the crack tip due to the DFZ, it is argued here that compared with the length scale over which SED is relevant to FCG (i.e., slip line length, micron-scale), the size and hence the effect of the DFZ (sub-micron scale) is trivial. Figure 4a and b illustrate this point. Based on the early work of Rice and Thomson [47], Wang et al. [48] presented an expression to quantify the impact of a single dislocation on local SIF, which is given by  $K_\theta^\perp = -\frac{3\mu b}{2(1-\nu)} \left( 2\pi r_{\text{avg}}^{-\frac{1}{2}} \right)$ , where  $r_{\text{avg}}$  is an averaged distance from the crack tip for  $n$  emitted dislocations, approximated in this paper as the slip line length,

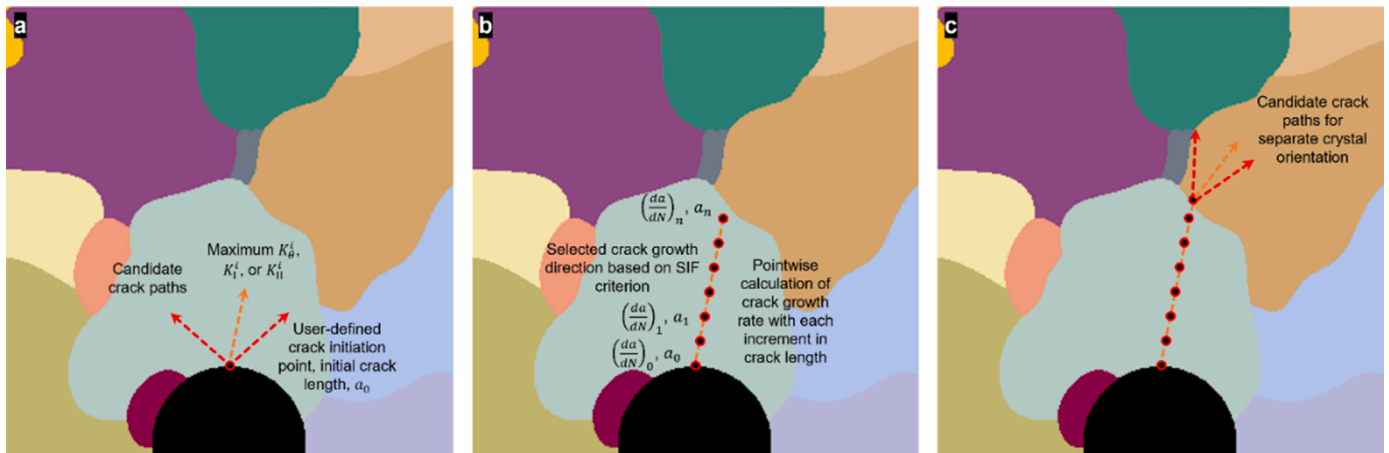


**Fig. 5.** Method for full-field polycrystalline implementation of analytical solution for FCG rate. a. Selection of crack path at the initiation stage based on (selected) crystallographic SIF-based criterion for short crack path. Since the crack path is simplified to be controlled by remote loading and crystallography alone, a single crack direction is assigned to each grain. b. Progression of crack along pre-defined path; at equally spaced intervals, the growth rate is computed. c. Upon traversing a grain boundary, a new crack direction is assigned and the process repeats.

$l_s$ . It is assumed that shielding dislocations only affect the SED contribution of slip system  $j$  due to the discrete nature of this model. The number of shielding dislocations,  $n$  is taken as an average of the number of dislocations emitted per cycle, such that the total dislocation shielding contribution for a given crack length is  $\Delta K_{\theta}^{\perp, \text{total}} = \Delta N \cdot n \cdot K_{\theta}^{\perp}$ , where  $\Delta N = \Delta a \cdot \left(\frac{da}{dN}\right)^{-1}$ . Accounting for dislocation shielding, Eq. (6) is now written as,

$$\frac{da}{dN} = \frac{l_s \cos(\theta^j)}{G_c} \cdot \xi \left( \sum_{i=1}^M \left[ \frac{4\tau_c^i b^i (1-2\nu)}{\pi\mu} \right]^{\frac{1}{2}} \cdot \Delta K_{\theta}^i + \left[ \frac{4\tau_c^j b^j (1-2\nu)}{\pi\mu} \right]^{\frac{1}{2}} \cdot \Delta K_{\theta}^{\perp, \text{total}} \right) \quad (7)$$

Since values for  $n$  correspond to the mean number of dislocations emitted from the crack tip per cycle, i.e., not accounting for pile-up effects,  $n$  is selected to maximise the cyclic dislocation shielding effect (for the initial crack length) in each case. Since the total shielding SIF is inversely proportional to FCG rate ( $\Delta K_{\theta}^{\perp, \text{total}} \propto \left(\frac{da}{dN}\right)^{-1}$ ), rearrangement of Eq. (7) gives a quadratic relationship between the mean number of emitted dislocations,  $n$  and  $\Delta K_{\theta}^{\perp, \text{total}}$ . There are two roots of such a relationship which give (i) a positive and (ii) a negative gradient,  $\frac{\partial n}{\partial \Delta K_{\theta}^{\perp, \text{total}}}$ . Naturally, a negative gradient is illogical since this suggests there is an increased shielding effect with decreasing  $n$ . Therefore, to maximise the shielding effect in a physically sensible manner, the inflection point is selected, for  $n$ , where  $\frac{\partial n}{\partial \Delta K_{\theta}^{\perp, \text{total}}} = 0$ , as described in Fig. 4c.

Mean dislocation spacing is calculated as  $l = \frac{l_s}{\Delta N_0 \cdot n}$ , and is used to estimate corresponding crack tip dislocation density assuming uniform dislocation spacing in 2D.  $\Delta N_0$  is the initial number of cycles before the crack propagates. Dislocation density is given by  $\rho_{\text{dis}} = \sqrt{l}/l$  for comparison with experimental crack tip measurements. Hence, the final model for FCG rate (Eq. (7)) is highly microstructure sensitive as it accounts for key microstructural material properties including crystal orientation, corresponding anisotropic elastic constants, slip properties, discrete slip directions, crack direction, and dislocation shielding effects. As noted in the previous section, unlike CPFE modelling, the analytical model does not account for grain-grain or crack-GB interactions but is instead aimed at capturing FCG rate trends in polycrystals, based on local crystallography and crack length alone. In addition, local crack path oscillations within individual grains are not captured using the current model, since the local stress state is unknown. In this paper, it is hypothesised that the dominant factors affecting FCG rate are related to

crystallography, and hence, that local crack path oscillations and interactions with microstructural features have little or no overall effect on the FCG rate trend.

#### 2.4. Crack path selection and full-field implementation in polycrystalline materials

To utilise the current model for full-field (2D free surface) crack path and FCG rate prediction within polycrystalline materials, a computer program is developed, whereby grain structure is defined using an image-based method. It is assumed that 2D grain structure information is sufficient for prediction of short FCG, and hence that substructural morphological variation is negligible, since the experimental crack growth rates and paths considered here were measured at the sample free surfaces. This assumption is further reinforced here by application to blocky alpha microstructures, which minimise substructural variations. Despite this assumption, full 3D grain orientations obtained from electron backscatter diffraction (EBSD) are used to account for crystallographic slip plane directions with respect to the loading conditions. In the experiments, notched beam samples measuring  $3 \times 3 \times 12$  mm were loaded in cyclic 3-point bending. Hence, in the bulk of the sample, rates of crack propagation are likely to vary in 3D (since even blocky alpha grains measuring 100 – 300  $\mu\text{m}$  are much smaller than total sample thickness). However, due to the strongly textured large-grain microstructures considered, it is reasonable to assume that substructural morphological variations are low (with respect to crack length), and hence, based on *St. Venant's principle*, that free-surface crack growth rates may be adequately described using 2D grain morphologies. The same assumptions apply to crack path prediction. Using CPFE modelling, criteria for short crack path are often controlled by maximum slip [37] or some related energy term [50]. However, since slip levels are not quantified using the current method, three crystallographic SIF-based criteria are proposed: (i) maximum shear SIF, combining modes I and II,  $\max(K_{II}^i)$ , (ii) maximum mode I SIF,  $\max(K_I^i)$ , and (iii) maximum mode II SIF,  $\max(K_{II}^i)$  (see Section 2.1 for details). The implementation of the maximum SIF method(s) is described in Fig. 5a. These new methods are compared in this paper to find a solution which gives greatest agreement with experimental crack paths. Hence, prediction of crack paths within polycrystalline microstructures will enable full-field implementation of the crack growth rate model for direct comparison with experiments. As shown in Fig. 5b., the method used here involves point-wise calculation of FCG rate within individual grains, tracking the spatial position of the crack tip as it extends.

A single crack propagation direction is defined for each crystal

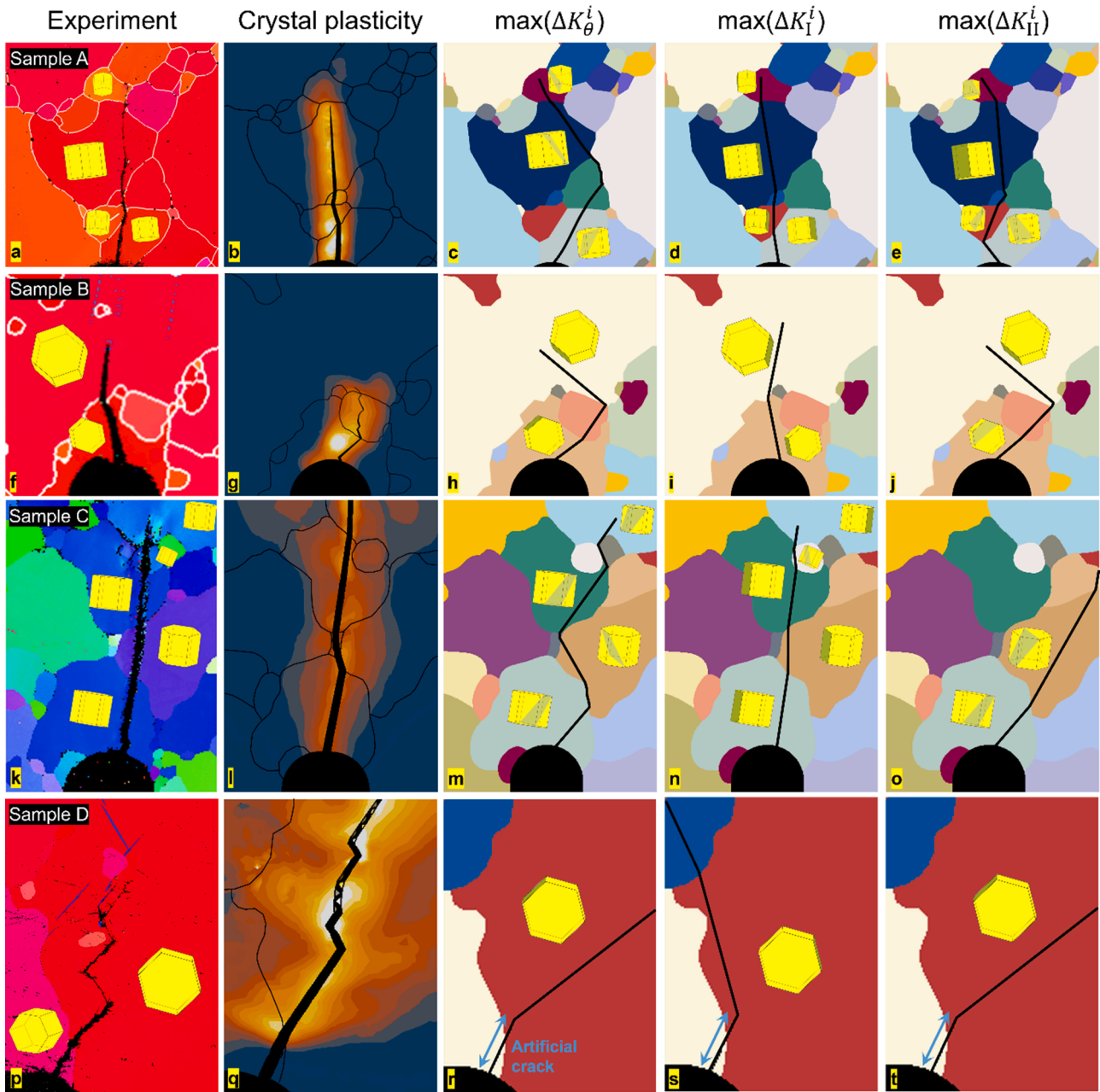


**Fig. 6.** Comparison of experimental crack path and CPFE simulation results with local SIF crack path prediction methods for a – e. Sample a. f – j, Sample b. k – o, Sample c. and p – t, Sample D. Maximum SIF criteria from left to right are maximum in-plane shear SIF, maximum mode I SIF, and maximum mode II SIF. CPFE simulations were carried out in previous work for Samples A and B [54] and C and D [37]. Local SIF criteria crack paths are presented alongside corresponding slip plane for each relevant grain.

orientation (or grain). Hence the crack growth rate will be governed by projected crack length, and crystallographic quantities (orientation, discrete slip etc.) corresponding to the crack tip position until such a point that the crack is detected to have traversed a grain boundary (Fig. 5c). Accordingly, grain-grain interactions and crack-grain interactions are unaccounted for using the current method (which, of course are accounted for, using CPFE modelling, for example). While such interactions are likely to have an effect, they are considered negligible in large-grain, strongly textured microstructures, such as those presented in this paper.

The program computes relevant in-plane elastic properties ( $\mu$  and  $\nu$ ) before the solver begins. This requires rotation of the  $6 \times 6$  compliance matrix,  $C$  according to the Euler angles of individual grains, using  $C' = MCM^T$ , where  $C'$  is the rotated compliance matrix, and  $M$  is the  $6 \times 6$

rotation matrix. For rotations about the a- and c-axis directions,  $M$  is given by Auld [51]. The solution for  $\frac{da}{dN}$  in Eq. (7) requires an explicit or iterative solving approach due to the self-dependence of input parameter,  $\Delta K_{\theta}^{\perp, \text{total}}$  on crack growth rate. Newton-Raphson iterative solving is used for this purpose. Lastly, for comparison with experiments, FCG is modelled in notched blocky alpha polycrystalline Zircaloy-4 samples which were loaded cyclically in 3-point bending (loading ratio,  $R = 0$ ). Hence, the remote SIF range is calculated using  $\Delta K^{\infty} = \frac{P}{B\sqrt{W}}f\left(\frac{a_e}{W}\right)$  from Anderson [52], where  $W$  and  $B$  are the sample width and thickness,  $P$  is the maximum applied force,  $S$  is the distance between the support pins and  $a_e$  is the effective crack length (notch length + projected crack length). The function,  $f\left(\frac{a_e}{W}\right)$  is given by,

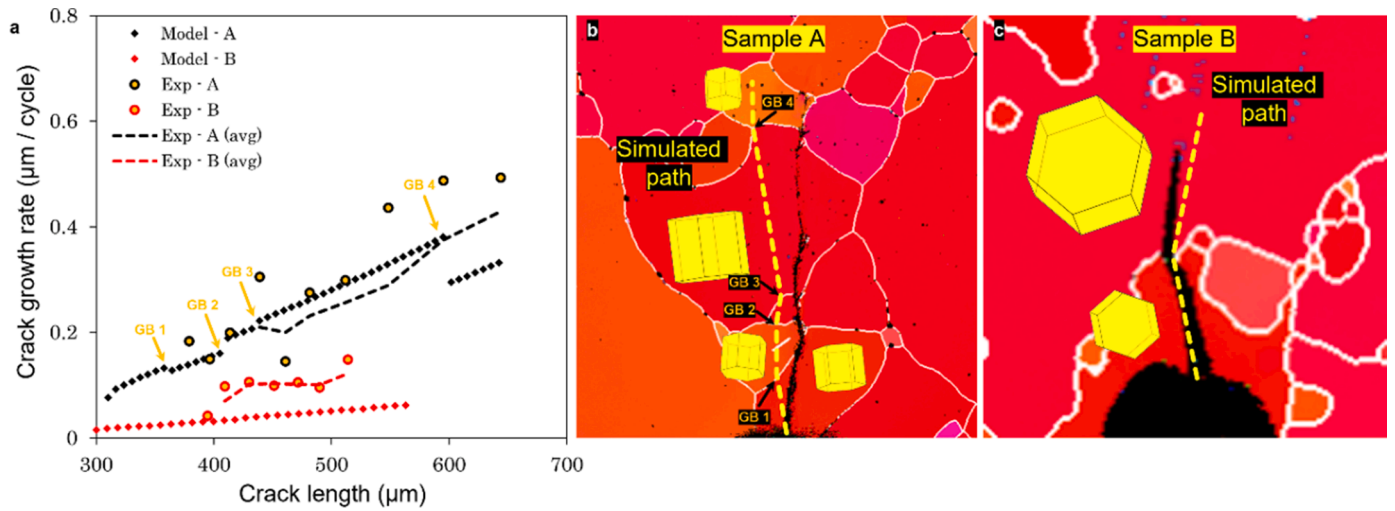


Fig. 7. Assessment of microstructural sensitivity of analytical solution. a. Comparison of analytical solution for FCG rate and experimental data for samples A and B. Comparison of predicted crack path using maximum mode I SIF criterion with experiment in b. sample A and c. sample B.

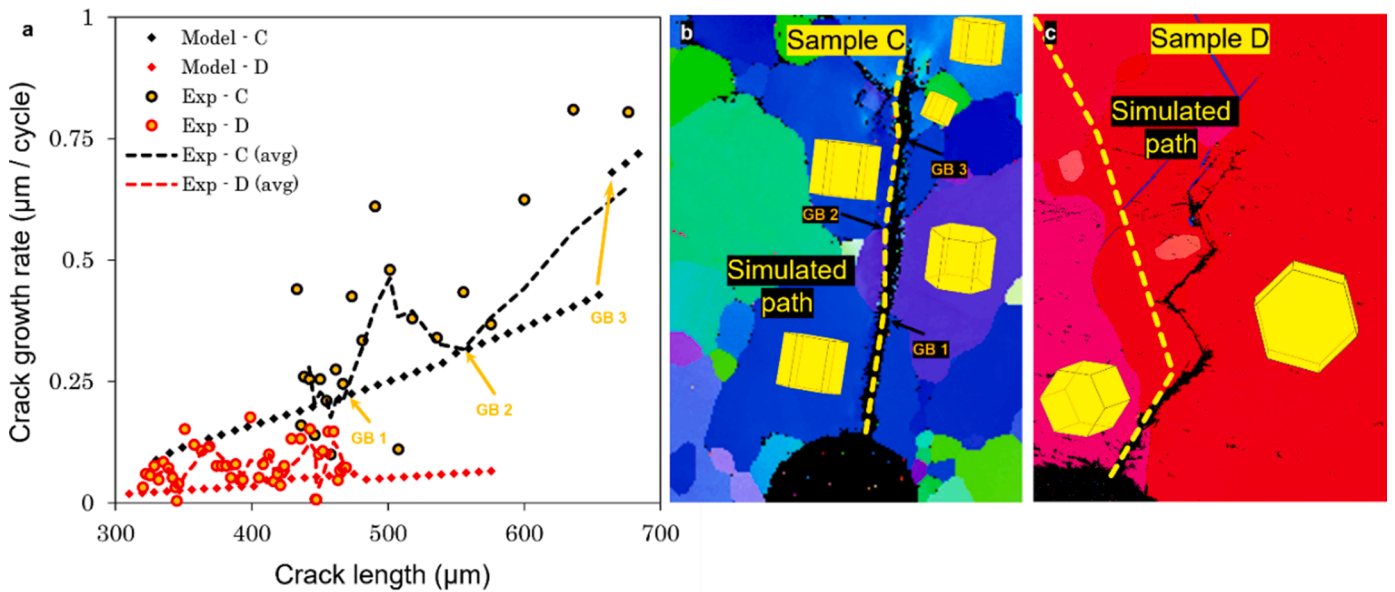


Fig. 8. Assessment of microstructural sensitivity of analytical solution. a. Comparison of analytical solution for FCG rate and experimental data for samples C and D. Comparison of predicted crack path using maximum mode I SIF criterion with experiment in b. sample C and c. sample D.

$$f\left(\frac{a_c}{W}\right) = \frac{3\left(\frac{S}{W}\right)\sqrt{\frac{a_c}{W}}}{2\left(1+2\frac{a_c}{W}\right)\left(1-\frac{a_c}{W}\right)^{\frac{3}{2}}}\left\{1.99-\frac{a_c}{W}\left(1-\frac{a_c}{W}\right)\left[2.15-3.93\left(\frac{a_c}{W}\right)+2.7\left(\frac{a_c}{W}\right)^2\right]\right\} \quad (8)$$

Equation (8) was derived from classical fracture mechanics test standards [53], with numerical coefficients corresponding to polynomial best-fitting. The method involved correlation of non-linearity of load-displacement data in 3-point bending with the known fracture toughness of various metallic materials. A summary of Zircaloy-4 material properties used within the FCG rate solution are provided in Appendix A.

### 3. Results and discussion

#### 3.1. Case study: crack path prediction and comparison with experiments

In this section, three crack path prediction methods based on local slip plane SIF are compared. Specifically, results from maximum SIF

crystallographic deformation mode ( $\Delta K_b^i$ ,  $\Delta K_I^i$ , and  $\Delta K_{II}^i$ ) criteria are compared with experiments and corresponding full-field CPFE-simulated crack paths (which use a maximum slip criterion) for selection of an optimal method which is subsequently used to compare FCG rates in polycrystalline Zircaloy-4. In Fig. 6, a comparison is made between the three candidate methods and experiments and CPFE simulation results. Samples were loaded in three-point bending, under cyclic  $R = 0$  loading conditions. Note that the CPFE contour fields presented in Fig. 6 represent the distribution of SED about the crack.  $\Delta K_I^i$  and  $\Delta K_{II}^i$  represent local slip plane mode I and mode II SIF ranges, as described in Fig. 2.

The CPFE maximum shear strain (slip) results [37,54] in Fig. 6b, g, l, q, demonstrate overall strong agreement with experiments. One exception to this rule, however, is for sample B, shown in Fig. 6g., where the maximum slip criterion predicts a very different crack path from the experiment (Fig. 6f). While the maximum slip criterion cannot be replicated within the new method (since the full-field stress state is unknown), the local SIF criterion which is most closely related to the maximum slip criterion is maximum  $\Delta K_b^i$ . This term accounts for both



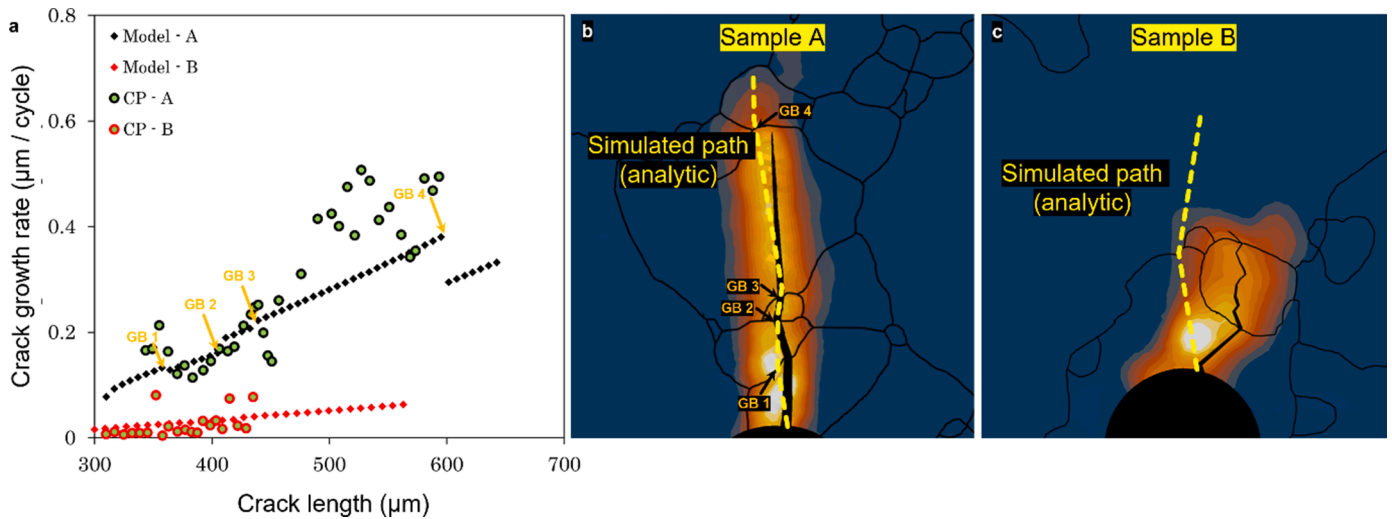


Fig. 9. a. Comparison of analytical solution for FCG rate and CPFE simulated data [54] for samples A and B. Comparison of predicted crack path using maximum mode I SIF criterion with CPFE maximum slip criterion in b. sample A and c. sample B. b,c, also display corresponding SED fields.

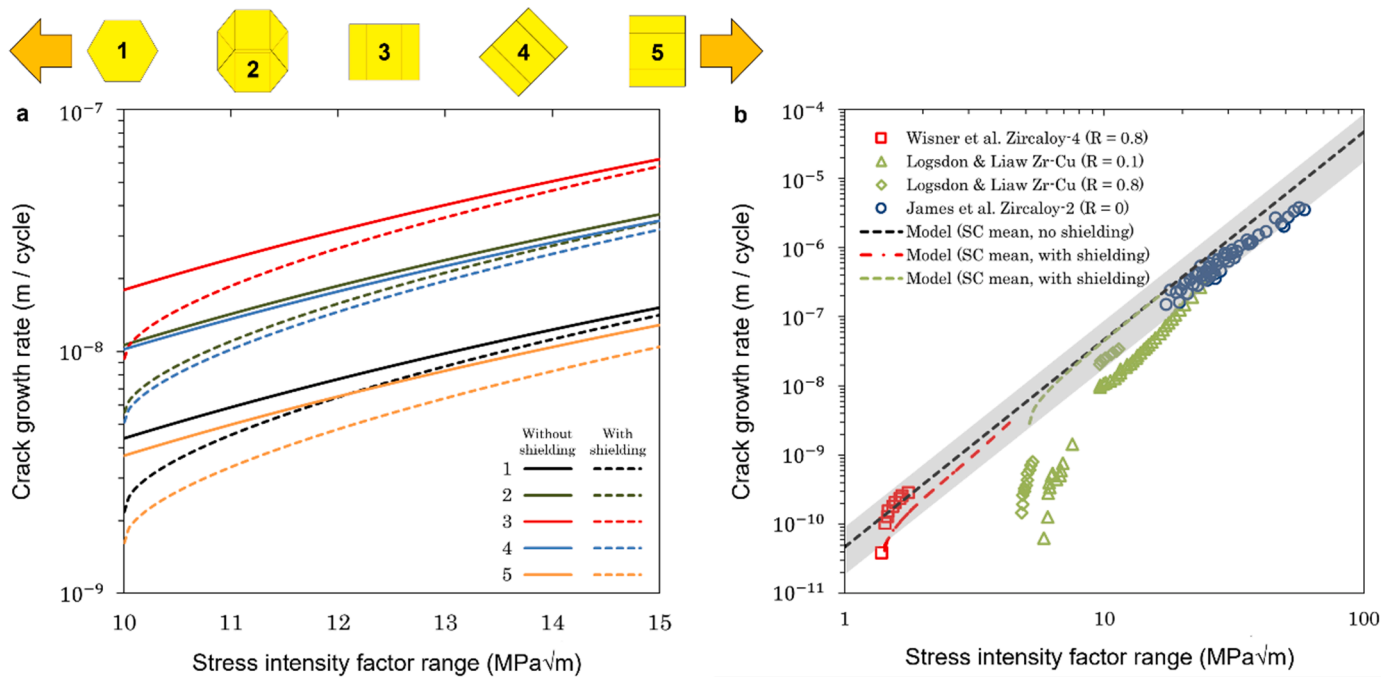


Fig. 10. Single crystal simulation results. a. Influence of crystal orientation and dislocation shielding model on SIF range-FCG rate relationship. Dashed lines correspond to the model with shielding included. Loading direction is indicated by arrows. Projected crack growth direction is vertical, relative to these crystal orientations. The vertical axis is presented in logarithmic scale. b. Comparison of single crystal (denoted SC) analytical model (with and without shielding) with experimental FCG rate data from literature [56–58]. Single crystal simulation results are based on the mean growth rates for orientations 1 – 5. Grey shaded region covers the total range of growth rates predicted for orientations 1 – 5 without dislocation shielding. Both axes are in logarithmic scale.

mode I and II SIF on the  $i$ th slip plane and is a measure of SIF along a slip line, constrained to lie on the free surface plane. For samples B and D, there is reasonable agreement between this method (Fig. 6h, r.) and the maximum slip criterion Fig. 6g, q), but much less so for samples A and C. This is because the Burgers vector directions of the dominant slip planes in samples B and D lie approximately within the free surface plane. Clearly, this is not true for samples A and C, since the CPFE-predicted crack paths are almost perpendicular to the remote loading direction. The maximum  $\Delta K_{II}^i$  criterion also tends to favour planes whose traces give  $\theta \sim 45^\circ$ ; this inadvertently results in grain boundary (GB) crack path oscillations in sample C (Fig. 6m). The maximum mode I SIF ( $\Delta K_I^i$ )

criterion for crack path demonstrates strong agreement with experiments. Indeed, this method gives more precise predictions than CPFE for samples B and C, but of course fails to capture clear crack path tortuosity within a single grain in sample D. Lastly, the maximum mode II SIF ( $\Delta K_{II}^i$ ) predictions are shown in Fig. 6e, j, o, t and compare poorly with experimental paths. In some regards,  $\Delta K_{II}^i$  performs better than  $\Delta K_{II}^i$  (e.g., grain 4 of sample A in Fig. 6e) but is clearly not the main driver for crack path. Hence, the maximum  $\Delta K_I^i$  criterion will be used for subsequent crack path and corresponding FCG rate predictions.

**Table 1**

Contributions of slip system groups to cyclic SED for a static crack with a SIF of  $10 \text{ MPa}\sqrt{\text{m}}$  under  $R = 0$  loading (without dislocation shielding). Contributions are represented as fractions of the total cyclic SED for each crystal orientation, i. e., as  $\dot{G}_{\text{sys}}/\dot{G}_{\text{total}}$ . Five single crystal orientations are considered with numbering and loading direction corresponding to those outlined in Fig. 10.

Orientation	Prismatic	Basal	Pyramidal <a>	Pyramidal <c+a>
1	0.2513	0	0.4754	0.2732
2	0.2608	0	0.4694	0.2698
3	0.1549	0	0.5367	0.3084
4	0.2053	0.2708	0.3327	0.1912
5	0	0	0.6350	0.3650

### 3.2. Case study: simulated crack growth rates and comparison with experiments

The analytical model for FCG rate, given by Eq. (7), is applied to samples A-D for comparison with experiments (using the property data in Appendix A), using the maximum  $\Delta K_I^c$  for crack path. Figure 7a shows that due to the strongly differing textures in samples A and B, there are vast differences in FCG rate. Reasons for this are discussed in the next section. The model effectively captures these differences. For sample A, there are also substantial growth rate fluctuations as the crack interacts with and crosses various microstructural features GB2 and GB3. These fluctuations are reflected by the analytical model, but rather subtly (compared with experiment), since the effect of the GB is not explicitly captured, as discussed previously. While it is clear that grain boundaries have a local effect (in the context of the current blocky alpha microstructures), the overall crack growth rate trends are reasonably well captured, which is the aim of the current work. Incorporation of grain-grain interactions is non-trivial, as there are morphological and crystallographic effects, as well as cyclic plasticity to consider. For example, depending on the orientation of one grain, i.e., set of crystallographic slip systems, with respect to another, slip blockage or transmission may occur. The Luster and Morris slip transfer parameter was used by Sudha et al. [55] to identify common slip transfer pairs between neighbouring grains based on TEM data after static tensile testing in a titanium alloy. Some such method could be applied here to capture microstructure interaction effects but would require sufficient statistical data for a given alloy, and hence, the model would no longer be deterministic.

Moreover, the growth rate transition across a GB is coarser than in the experiment since the model has no knowledge of the GB until it is crossed. In the final grain of sample A, a substantial drop in FCG rate is predicted, which reflects the experimental data, though not entirely for the reasons outlined above. While the link between FCG rate and GBs is less clear for sample B, the growth rate trend is effectively captured using the model, despite under-predicting it somewhat.

In terms of texture, samples C and D are very similar to samples A and B, respectively, and hence, rates of growth are significantly higher in C than D, as shown in Fig. 8a. As before, the analytical model captures the general trend for each sample but does not capture substantial FCG rate fluctuations. The larger fluctuations here are likely due to greater anisotropy between neighbouring grains in sample C, than in A. Interestingly, after the crack crosses GB3 of sample C, there is a substantial increase in rate due to the orientation of the fourth grain, increasing to values comparable with the experiment. FCG rates are partially under-predicted by the model for each of these samples. This could be corrected by adjusting the critical SED,  $G_c$ , but is not, in order to maintain consistency with CPFE modelling [54]. Adjusting  $G_c$  is unlikely to reflect the true mechanistic driver of these differences, since localisation of SED along GBs is anticipated to be the dominant factor.

The overall growth rate magnitude in sample D is captured by the model, but as with previous samples, fluctuations are not. In this case, crack path tortuosity is likely to be the driver of these fluctuations, which cannot be captured using the current technique. An important factor to consider in these results, as with the CPFE results, is that all

crack path and crack growth rate results are determined using free surface EBSD data. Hence, there are potentially 3D, i.e., substructure effects, which contribute towards differences between experiment and model. Despite this, the 2D approximation is valid at the free surface, assuming plane stress conditions, and enables reasonably accurate predictions of short crack growth rate and path.

For samples A and B, CPFE simulated crack paths and rates are compared with the analytical model. Figure 9a shows strong agreement between both simulation methods in terms of rate for both samples, despite differences in crack path, which are shown clearly in Fig. 9b and c.

Given the simplicity of the current crack path prediction method, it is surprising that it achieves much greater agreement with experiment than the CPFE result. However, full-field CPFE predictions are more sensitive than the current method to microstructure interactions, enabling more precise growth rate predictions (where the crack path is successfully captured). Furthermore, it is important to note that to generate the CPFE data presented, it took between 5,000–10,000 CPU hours, compared with mere seconds for the analytical model. Both numerical and analytical simulations were carried out using Intel Gold 6152 processors at 2.10 GHz. 16 cores and 8 GB of RAM were assigned to each job.

### 3.3. Influence of crystal orientation and dislocation shielding with application to stage II cracks

The model is applied to Zircaloy-4 single crystals to study the influence of orientation on FCG rate. Five orientations are selected to broadly capture the material behaviour. The influence of dislocation shielding is studied by comparing rates of FCG with and without shielding, i.e., where  $K_{\theta}^{\perp} = 0$ , in the SIF range  $10\text{--}15 \text{ MPa}\sqrt{\text{m}}$ . A comparison of these results is presented in Fig. 10.

Figure 10a shows that the model predicts very strong microstructural sensitivity in terms of growth rate, with rates in orientation 3 greater than orientation 5 by more than a factor of 6. Growth rate is highest in orientation 3 due to its elastic properties contributing to highest cyclic SED and favourable orientation and length of the dominant slip line. While the in-plane elastic properties are the same for orientation 5, growth rate is compromised due to there being no basal or prismatic contribution to SED since basal planes lie perpendicular to the remote loading direction, and prismatic planes lie parallel. This leaves highly inclined pyramidal planes to control crack direction, meaning that the projected crack extension ( $\Delta a$ ) is relatively low. FCG rates for orientation 1 are comparably low due to elastic properties giving low cyclic SED as well as high prismatic slip plane inclination. Orientations 2 and 4 are predicted to have similar growth rate trends due to a combination of the factors discussed. Results also highlight the influence of dislocation shielding on FCG rate. Within the SIF range studied, dislocation shielding reduces growth rate by approximately 20%. More importantly, the model captures that shielding has the greatest influence initially (at lowest SIF). Values for mean number of dislocations emitted per cycle range between 6 and 42. Equivalent dislocation densities are estimated to be between  $4000\text{--}5000 \mu\text{m}^{-2}$ . These estimates are consistent with experimental X-ray diffraction (XRD) measurements of dislocation densities at crack tips [59] ( $\sim 2500 \mu\text{m}^{-2}$ ).

To understand the influence of the various HCP slip systems in Zircaloy-4, their contributions to cyclic SED are presented in Table 1, as fractions of total cyclic SED for a given crack length and loading conditions. The variation of contributions is compared across the five single crystal orientations considered in Fig. 10.

Table 1 shows that on average, according to the current model, the greatest contributors to cyclic SED in HCP Zircaloy-4 are the <a> pyramidal slip systems, followed by <c+a> pyramidal, prismatic, and basal. The pyramidal contributors are largest due (primarily) to there being 6 <a and 12 <c+a> systems, while there are just 3 prismatic and basal systems, respectively. Hence, normalised results would indicate

that on average, prismatic systems make the greatest individual contributions to cyclic SED, i.e., undergo maximum slip activity, which is consistent with experiments [60] and modelling [38]. The relatively low combined contribution of  $\langle c+a \rangle$  slip systems to cyclic SED is due to the comparably high CRSS (see Appendix A: Material properties).

The universality of the model is assessed through comparison with experimental FCG rate data over a wide SIF range. Wisner et al. [57] tested the fatigue behaviour of Zircaloy-4 at low SIF values (in the range 1–2 MPa $\sqrt{m}$ ). Precise crystallographic details of samples are unavailable, but Kearns factors [61] were of the order of 0.7. Logsdon and Liaw [58] tested a Zr-Cu alloy (Zr content >99%) in the SIF range 5–30 MPa $\sqrt{m}$  with loading ratios 0.1 and 0.8. James [56] carried out room temperature tests on Zircaloy-2 in the range 10–60 MPa $\sqrt{m}$  in samples where the crack direction was either orthogonal to or parallel to the sheet rolling direction. Minimal growth rate variation was observed between samples, particularly for high SIFs, indicating low microstructure-sensitivity. A comparison of the experimental FCG data mentioned above with the analytical model (with and without shielding) is presented in Fig. 10b, using generalised mean single crystal results. The comparison shows strong agreement between the model and experiments, despite obvious differences in microstructure and composition. Unsurprisingly, strongest agreement is attained with Zircaloy-4 data from Wisner et al. [57], excluding for lower SIF ranges. However, application of the dislocation shielding model is shown to capture some of the experimental ‘starting’ FCG behaviour, while somewhat under-predicting magnitude. Similarly, Zr-Cu FCG rates are over-predicted, but application of the shielding model also captures the transition from ‘starting’ to Paris’ law [2] behaviour. This crack growth starting behaviour is captured for a range of initial SIF values and is akin to the asymptotic thresholding behaviour observed in many materials, whereby for decreasing values of SIF range, cracks cease to propagate [62]; the threshold SIF range is denoted  $\Delta K_{th}$ . Fig. 10b demonstrates that as the initial or starting value for SIF range is decreased, the shielding behaviour becomes more dramatic. However, this does not indicate that there is some threshold value which can be predicted using the current model; rather, it captures the phenomenon to an extent, as predicted growth rates reach as low as single atomic lattice spacings per cycle. Incorporation of additional physics-based understanding of dislocation emission from the crack tip, rather than the mean approach incorporated here, may however allow for this behaviour to be captured more precisely.

In addition, the model appears to capture loading ratio effects, despite not accounting for loading ratio explicitly. Effectively, the SIF range helps to capture the cyclic behaviour, while the slip line length,  $l_s$ , accounts for the peak SIF magnitude. In combination, these factors represent a loading ratio effect. Lastly, Zircaloy-2 FCG data is shown to lie within the growth rate range (shaded grey region), even for high values of  $\Delta K^\infty$ , demonstrating that the model has the potential to capture stage II FCG behaviour.

#### 4. Conclusion

A deterministic analytical model has been developed, which is a

#### Appendix A. Material properties

The Zircaloy-4 material properties used in the FCG rate model are summarised in Table A1. The key parameters for crack growth are the critical SED,  $G_c$ , and the fraction of plastic strain energy stored in dislocation structure,  $\xi$ . The critical SED was obtained by Long et al. [54] using CPFE modelling of crack growth through Zircaloy-4 microstructures. By scaling the arbitrarily selected CPFE value for  $G_c$  against the ratio of experimental to simulated crack growth rates, an estimate for the true critical SED was obtained. The fraction of plastic strain energy density, which is assumed constant, is taken as 5%, and is consistent with previous modelling work [54]. The remaining 95% of plastic strain energy is assumed to disperse into the environment as heat etc. [41].

prospective candidate for prediction of short crack growth rates in a range of ductile metallic materials. It is evident that SED, which forms the basis for the model, can effectively capture the effect of key microstructural characteristics (elastic anisotropy, discrete slip, etc.) on FCG rate. The development of a new crack path prediction tool based on maximum (slip plane-based) mode I SIF, in combination with the analytical solution was shown to capture overall FCG rate trends and crack paths in a range of Zircaloy-4 polycrystals, and to even outperform CPFE (maximum slip-based) crack path predictions in some instances. Furthermore, a distinct advantage of the analytical model over numerical, e.g., CPFE calculations, is the substantial reduction in computer processing requirements; solving times using the analytical approach are of the order of CPU-seconds, compared with thousands of CPU-hours required using numerical methods. Finally, application of the model to stage II FCG data from the literature demonstrates its versatility, as it showed strong agreement with the data within a broad range of  $\Delta K$  values. The comparison also demonstrates the ability of the dislocation shielding term to capture the transition from fatigue ‘starting’ behaviour through to stage I or II crack growth.

#### CRediT authorship contribution statement

**Daniel J. Long:** Methodology, Software, Validation, Formal analysis, Writing – original draft. **Yang Liu:** Methodology, Writing – review & editing. **Weifeng Wan:** Investigation. **Fionn P.E. Dunne:** Conceptualization, Resources, Writing – review & editing, Supervision, Project administration, Funding acquisition.

#### Declaration of Competing Interest

The authors declare the following financial interests/personal relationships which may be considered as potential competing interests: Daniel J Long reports financial support was provided by Engineering and Physical Sciences Research Council. Daniel J Long reports financial support was provided by Rolls-Royce plc. Daniel J Long reports a relationship with Rolls-Royce plc that includes: non-financial support.

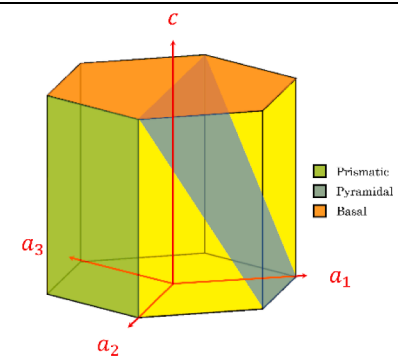
#### Data availability

Data will be made available on request.

#### Acknowledgments

The authors wish to acknowledge the Engineering and Physical Sciences Research Council and Rolls-Royce plc for their financial contributions to this research work. DJL and FPED would also like to express gratitude to Rolls-Royce plc for their advice relating to the modelling work presented in this paper.

**Table A1**  
Key quantities used in analytical solution for crack growth rate for Zircaloy-4.

Parameter	Value	Unit	HCP crystallography
$G_c$	250	J / m <sup>2</sup>	
$\xi$	0.05	-	
$\tau_{c,prism(a)}$	153	MPa	
$\tau_{c,pyramid(a)}$	153	MPa	
$\tau_{c,pyramid(c+a)}$	532.4	MPa	
$\tau_{c,basal(a)}$	203.5	MPa	
$b_{(a)}$	$3.2 \cdot 10^{-4}$	$\mu\text{m}$	
$b_{(c+a)}$	$5.1 \cdot 10^{-4}$	$\mu\text{m}$	
$\nu_a$	0.4006	-	
$\nu_c$	0.2375	-	
$\mu_a$	35.1	GPa	
$\mu_c$	32.0	GPa	

Subscripts (a) and (c) represent hexagonal close packed (HCP) a- and c-axis directions, respectively.

The crystallographic slip strengths are also given in Table A1 and were adopted from pillar test measurements of pure Zirconium by Gong et al. [63]. Further, direct CPFEE modelling of experimental creep tests [64] were used to validate these slip properties at the microstructural scale. Due to non-availability of the <a> pyramidal slip strength, its value is assumed equal to the prismatic value, which was demonstrated to give agreement with experiments [64].

**Appendix B. Full-field implementation of model in polycrystals**

Simulations using the analytical solution are carried out within commercial software, MATLAB. Several user inputs including grain orientation, initial crack length, and position are required before the program can run, as outlined in Fig. B1.

Rotations of the anisotropic 6 × 6 compliance matrix, C according to the Euler angles of individual grains, are carried out about the a-directions using the rotation matrix given by Supplementary Equation (B1).

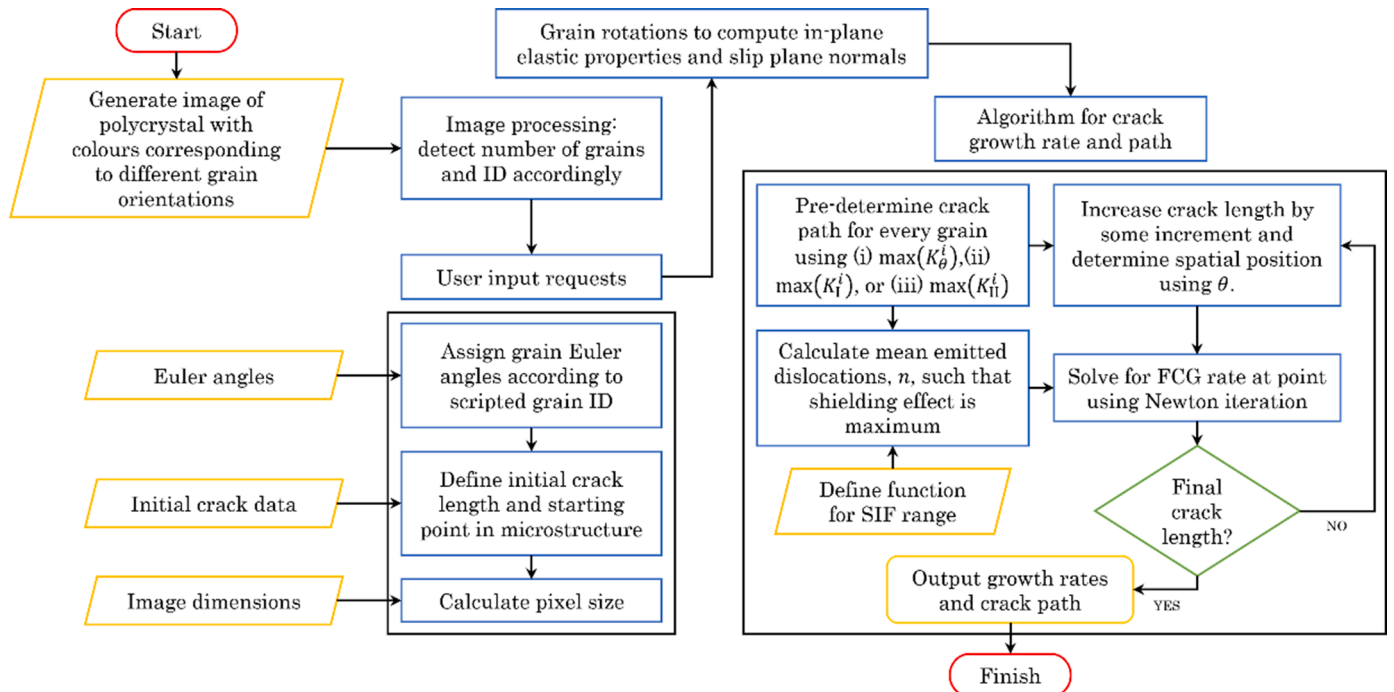


**Fig. B1.** Flowchart describing algorithm and full-field implementation of analytical FCG rate solution with crack path prediction.

$$\mathbf{M} = \begin{bmatrix} 1 & 0 & 0 & 0 & 0 & 0 \\ 0 & \cos^2\psi & \sin^2\psi & \sin 2\psi & 0 & 0 \\ 0 & \sin^2\psi & \cos^2\psi & -\sin 2\psi & 0 & 0 \\ 0 & \frac{\sin\psi}{2} & \frac{\sin 2\psi}{2} & \cos 2\psi & 0 & 0 \\ 0 & 0 & 0 & 0 & \cos\psi & -\sin\psi \\ 0 & 0 & 0 & 0 & \sin\psi & \cos\psi \end{bmatrix} \quad (\text{B1})$$

where  $\psi$  is an Euler angle. For c-axis (crystal coordinate system) rotations through angle  $\varphi$ ,  $\mathbf{M}$  is given by,

$$\mathbf{M} = \begin{bmatrix} \cos^2\varphi & \sin^2\varphi & 0 & 0 & 0 & \sin 2\varphi \\ \sin^2\varphi & \cos^2\varphi & 0 & 0 & 0 & -\sin 2\varphi \\ 0 & 0 & 1 & 0 & 0 & 0 \\ 0 & 0 & 0 & \cos\varphi & -\sin\varphi & 0 \\ 0 & 0 & 0 & \sin\varphi & \cos\varphi & 0 \\ -\frac{\sin 2\varphi}{2} & \frac{\sin\varphi}{2} & 0 & 0 & \sin\varphi & \cos 2\varphi \end{bmatrix} \quad (\text{B2})$$

### Appendix C. CPFEE modelling description

The CPFEE modelling methodology for some of the work presented in this paper has been presented in greater detail previously [37,54]. A brief summary of the methodology is provided here. CPFEE modelling is used to capture micro-scale elastic-plastic deformation. A user-material (UMAT) subroutine code is implemented within commercial finite element software, Abaqus. The key equation which links dislocation slip activation with plastic deformation at the microstructural level is given by,

$$\dot{\gamma}^i = \rho_m \nu b^2 \exp\left(\frac{-\Delta F}{k_B T}\right) \sinh\left(\frac{(\tau^i - \tau_c^i) \Delta V}{k_B T}\right) \quad (\text{C1})$$

where  $\dot{\gamma}^i$  is the slip rate on the  $i$ th slip system,  $\rho_m$  is the density of mobile dislocations,  $\nu$  is the frequency of attempts of dislocations to surmount the thermal energy barrier,  $\Delta F$  is the activation energy,  $T$  is temperature,  $\tau^i$  is the local resolved shear stress of the  $i$ th slip system, and  $\Delta V$  is activation volume. Using Schmid's Law, the plastic velocity gradient is calculated via the contributions of each slip system. In addition, Eq. (C1) is used to predict crack path within the CPFEE modelling methodology, as it is the slip system with maximum shear strain (slip) which controls crack path.

Since CPFEE is a numerical method, quantities such as total slip for a given slip system are computed locally and incrementally, using numerical integration, giving spatial and temporal resolution. Similarly, SED is calculated within the CPFEE code using numerical integration of SED increments as follows,

$$G = \xi \int \frac{\boldsymbol{\sigma} : d\mathbf{e}^p}{\sqrt{\rho_{\text{SSD}} + \rho_{\text{GND}}}} \quad (\text{C2})$$

where  $\boldsymbol{\sigma}$  is the 3D stress tensor and  $d\mathbf{e}^p$  is the plastic strain increment tensor.  $\rho_{\text{SSD}}$  and  $\rho_{\text{GND}}$  represent the densities of sessile and geometrically necessary dislocations, respectively. Implementation of the above methodology is performed via the UMAT subroutine also. For simulation of polycrystalline materials, the orientation of each grain is represented explicitly. An example is given in Fig. C1 below.

Figure C1 describes the methodology used to represent real microstructures from experiments. In the current and previous work, 2D EBSD data were used to represent microstructures of free surfaces. While CPFEE modelling is technically 3D, the free surface microstructures are simply extruded in the out-of-plane direction over a sufficient thickness to represent plane stress conditions. Similarly, although crystallographic plane orientations were used to control crack path direction, only the free surface components are accounted for in this work. Crack growth is enabled here using XFEM, with the SED fracture criterion.

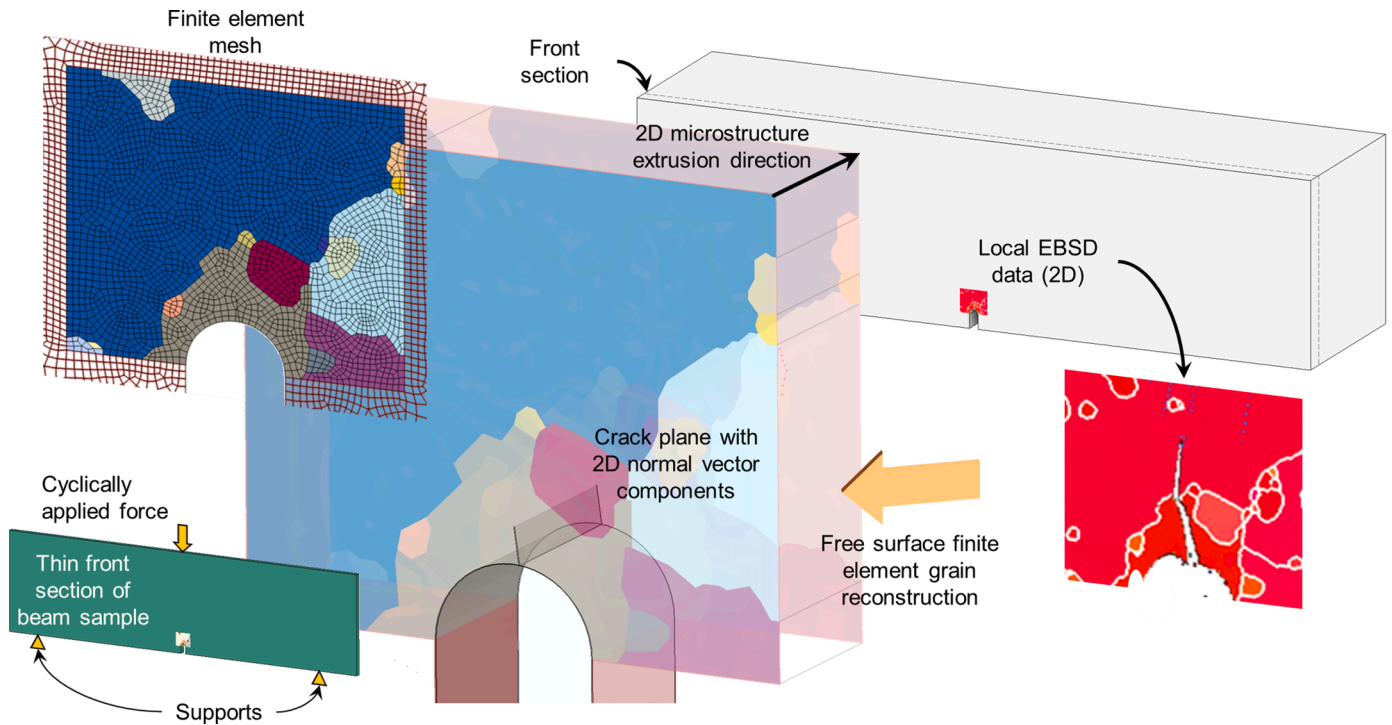


**Fig. C1.** Structure of CPFE model for representation of experimental 3-point-bending. Detail of microstructure within the region of interest is obtained using electron backscatter diffraction (EBSD) measurements. The region of interest is reconstructed in 2D within a finite element model and is extruded linearly in the out-of-plane direction. Elastic-plastic property data are assigned to the rest of the beam.

## References

- [1] Ewalds HL, Wanhill RJH. *Fracture mechanics*. 4th ed. London: Edward Arnold; 1989.
- [2] Paris PC, Gomez MP, Anderson WEP. A Rational analytic theory of fatigue. *Trend Eng* 1961;13:9–14. <https://doi.org/10.11648/j.ijmea.s.2015030201.11>. *Trend Eng*.
- [3] Cockeram BV, Kammenzind BF. The increase in fatigue crack growth rates observed for Zircaloy-4 in a PWR environment. *J Nucl Mater* 2018;499:111–25. <https://doi.org/10.1016/j.jnucmat.2017.11.015>.
- [4] Cattivelli A, Roy MJ, Burke MG, Dhers J, Lee TL, Francis JA. Internal stresses in a clad pressure vessel steel during post weld heat treatment and their relevance to underclad cracking. *Int J Pressure Vessels Piping* 2021;193:104448. <https://doi.org/10.1016/j.ijpvp.2021.104448>.
- [5] Reed PAS, Wu XD, Sinclair I. Fatigue crack path prediction in UDIMET 720 nickel-based alloy single crystals. *Metall Mater Trans A Phys Metall Mater Sci* 2000;31(1):109–23. <https://doi.org/10.1007/s11661-000-0058-6>.
- [6] Zheng Z, Zhao P, Zhan M, Shen S, Wang Y, Fu MW. The roles of rise and fall time in load shedding and strain partitioning under the dwell fatigue of titanium alloys with different microstructures. *Int J Plast* 2022;149. <https://doi.org/10.1016/j.ijplas.2021.103161>. Feb.
- [7] Poon CT, Barrett RA, Leen SB. Global and local modeling for inter-wire fretting in multi-wire copper conductors. *Fatigue Fract Eng Mater Struct* 2022;45(6):1618–34. <https://doi.org/10.1111/ffe.13683>. Jun.
- [8] Texier D, et al. Short crack propagation from cracked non-metallic inclusions in a Ni-based polycrystalline superalloy. *Acta Mater* 2019;165:241–58. <https://doi.org/10.1016/j.actamat.2018.11.051>. Feb.
- [9] Zhang L, Zhao LG, Roy A, Silberschmidt Vv, McColvin G. In-situ SEM study of slip-controlled short-crack growth in single-crystal nickel superalloy. *Mater Sci Eng A* 2019;742:564–72. <https://doi.org/10.1016/j.msea.2018.11.040>. Jan.
- [10] Milan MT, Spinelli D, Bose Filho WW, Montezuma MFV, Tita V. Failure analysis of a SAE 4340 steel locking bolt. *Eng Fail Anal* 2004;11(6):915–24. <https://doi.org/10.1016/j.engfailanal.2003.12.003>.
- [11] McDowell DL. *Basic issues in the mechanics of high cycle metal fatigue*. *Int J Fract* 1996;80:103–45.
- [12] Wen W, Cai P, Ngan AHW, Zhai T. An experimental methodology to quantify the resistance of grain boundaries to fatigue crack growth in an AA2024 T351 Al-Cu Alloy. *Mater Sci Eng A* 2016;666:288–96. <https://doi.org/10.1016/j.msea.2016.04.071>.
- [13] Zhai T, Wilkinson AJ, Martin JW. Crystallographic mechanism for fatigue crack propagation through grain boundaries. *Acta Mater* 2000;48(20):4917–27. [https://doi.org/10.1016/S1359-6454\(00\)00214-7](https://doi.org/10.1016/S1359-6454(00)00214-7).
- [14] Sangid MD, Ezaz T, Sehitoglu H, Robertson IM. Energy of slip transmission and nucleation at grain boundaries. *Acta Mater* 2011;59(1):283–96. <https://doi.org/10.1016/j.actamat.2010.09.032>. Jan.
- [15] Chowdhury PB, Sehitoglu H, Rateick RG, Maier HJ. Modeling fatigue crack growth resistance of nanocrystalline alloys. *Acta Mater* 2013;61(7):2531–47. <https://doi.org/10.1016/j.actamat.2013.01.030>. Apr.
- [16] Chowdhury PB, Sehitoglu H, Rateick RG. Predicting fatigue resistance of nano-twinned materials: Part I - Role of cyclic slip irreversibility and Peierls stress. *Int J Fatigue* 2014;68:277–91. <https://doi.org/10.1016/j.ijfatigue.2014.05.014>.
- [17] Chowdhury PB, Sehitoglu H, Rateick RG. Predicting fatigue resistance of nano-twinned materials: Part II - effective threshold stress intensity factor range. *Int J Fatigue* 2014;68:292–301. <https://doi.org/10.1016/j.ijfatigue.2014.06.006>.
- [18] Zhang P, Zhang L, Baxevanakis KP, Zhao LG, Bullough C. Modelling short crack propagation in a single crystal nickel-based superalloy using crystal plasticity and XFEM. *Int J Fatigue* 2020;136. <https://doi.org/10.1016/j.ijfatigue.2020.105594>. Jul.
- [19] Dawson PR. *Computational crystal plasticity*. *Int J Solids Struct* 2000;37:115–30.
- [20] Shen J, Kotha S, Noraas R, Venkatesh V, Ghosh S. Developing parametrically upscaled constitutive and crack nucleation models for the  $\alpha/\beta$  Ti64 alloy. *Int J Plast* 2022;151. <https://doi.org/10.1016/j.ijplas.2021.103182>. Apr.
- [21] Grilli N, Tarleton E, Cocks ACF. Coupling a discrete twin model with cohesive elements to understand twin-induced fracture. *Int J Fract* 2021;227(2):173–92. <https://doi.org/10.1007/s10704-020-00504-9>.
- [22] Remmers JJC, de Borst R, Needleman A. The simulation of dynamic crack propagation using the cohesive segments method. *J Mech Phys Solids* 2008;56(1):70–92. <https://doi.org/10.1016/j.jmps.2007.08.003>.
- [23] Zhao Q, Abdel Wahab M, Ling Y, Liu Z. Fatigue crack propagation across grain boundary of Al-Cu-Mg bicrystal based on crystal plasticity XFEM and cohesive zone model. *J Mater Sci Technol* 2022;126:275–87. <https://doi.org/10.1016/j.jmst.2022.03.020>. Nov.
- [24] Dolbow J, Moës N, Belytschko T. Discontinuous enrichment in finite elements with a partition of unity method. *Finite Elem Anal Des* 2000;36(3):235–60. [https://doi.org/10.1016/S0168-874X\(00\)00035-4](https://doi.org/10.1016/S0168-874X(00)00035-4).
- [25] Silling SA. Reformulation of elasticity theory for discontinuities and long-range forces. *J Mech Phys Solids* 2000;48(1):175–209. [https://doi.org/10.1016/S0022-5096\(99\)00029-0](https://doi.org/10.1016/S0022-5096(99)00029-0).
- [26] Bangboye A, Haynes TA, Wenman MR. Predicting crack patterns in SiC-based cladding for LWR applications using peridynamics. *Procedia Struct Integr* 2020;28:1520–35. <https://doi.org/10.1016/j.prostr.2020.10.125>.
- [27] Karpenko O, Oterkus S, Oterkus E. Titanium alloy corrosion fatigue crack growth rates prediction: peridynamics based numerical approach. *Int J Fatigue* 2022;162:107023. <https://doi.org/10.1016/j.ijfatigue.2022.107023>.
- [28] Hong K, Oterkus S, Oterkus E. Peridynamic analysis of fatigue crack growth in fillet welded joints. *Ocean Eng* 2021;235:109348. <https://doi.org/10.1016/J.OCEANENG.2021.109348>. Sep.
- [29] Wang D, Zhao L, Xu L, Han Y, Hao K. A microstructure-based study of irradiation hardening in stainless steel: experiment and phase field modeling. *J Nucl Mater* 2022;569:153940. <https://doi.org/10.1016/j.jnucmat.2022.153940>.

- [30] Ai W, Wu B, Martínez-Pañeda E. A coupled phase field formulation for modelling fatigue cracking in lithium-ion battery electrode particles. *J Power Sources* 2022; 544:231805. <https://doi.org/10.1016/j.jpowsour.2022.231805>.
- [31] Montes de Oca Zapian D, Stewart JA, Dingreville R. Accelerating phase-field-based microstructure evolution predictions via surrogate models trained by machine learning methods. *NPJ Comput Mater* 2021;7(1):3. <https://doi.org/10.1038/s41524-020-00471-8>.
- [32] Zhou H, Suzuki Y, Kinofuchi M, Schmauder S, Dogahe K, Shibamura K. Bridging strategy between microscopic and macroscopic crack growth simulations to predict fatigue strength of steels. *Int J Fatigue* 2023;168. <https://doi.org/10.1016/j.ijfatigue.2022.107386>. Mar.
- [33] Zhou H, Liu Z, Kinofuchi M, Shibamura K. Multiscale modelling strategy for predicting fatigue lives and limits of steels based on a generalised evaluation method of grain boundaries effects. *Int J Fatigue* 2022;158. <https://doi.org/10.1016/j.ijfatigue.2022.106749>. May.
- [34] Zhou H, Liu Z, Kikuchi S, Shibamura K. Analysis of fatigue performance of austenitic stainless steels with bimodal harmonic structures based on multiscale model simulations. *Mater Des* 2023;111657. <https://doi.org/10.1016/j.matdes.2023.111657>. Feb.
- [35] Ito H, Suzuki Y, Nishikawa H, Kinofuchi M, Enoki M, Shibamura K. Multiscale model prediction of ferritic steel fatigue strength based on microstructural information, tensile properties, and loading conditions (no adjustable material constants). *Int J Mech Sci* 2020;170. <https://doi.org/10.1016/j.ijmesci.2019.105339>. Mar.
- [36] Griffith AA. The phenomena of rupture and flow in solids. *R Soc* 1921;221 (582–593):163–98. <https://doi.org/10.1098/rsta.1921.0006>.
- [37] Wilson D, Wan W, Dunne FPE. Microstructurally-sensitive fatigue crack growth in HCP, BCC and FCC polycrystals. *J Mech Phys Solids* 2019;126:204–25. <https://doi.org/10.1016/j.jmps.2019.02.012>.
- [38] Xu Y, Wan W, Dunne FPE. Microstructural fracture mechanics: stored energy density at fatigue cracks. *J Mech Phys Solids* 2021;146(August 2020):104209. <https://doi.org/10.1016/j.jmps.2020.104209>.
- [39] Recho N. *Fracture mechanics and crack growth*. London Hoboken, N.J: Wiley-ISTE; 2012. 1. Aufl.
- [40] Wan VVC, Maclachlan DW, Dunne FPE. A stored energy criterion for fatigue crack nucleation in polycrystals. *Int J Fatigue* 2014;68:90–102. <https://doi.org/10.1016/j.ijfatigue.2014.06.001>.
- [41] Čebren M, Kosel F. Stored energy predictions from dislocation-based hardening models and hardness measurements for tensile-deformed commercial purity copper. *Strojnikski Vestnik/J Mech Eng* 2014;60(7–8):462–74. <https://doi.org/10.5545/sv-jme.2013.1569>.
- [42] Gdoutos EE. *Fracture mechanics criteria and applications*. Dordrecht: Kluwer Academic Publishers; 1990.
- [43] Pan J, Lin SH. *Fracture mechanics and fatigue crack propagation*. 1st ed. Elsevier Inc.; 2005. <https://doi.org/10.1016/B978-075067719-6/50007-5>.
- [44] Liang S, Zhu Y, Huang M, Li Z. Studying dislocation-induced shielding effect on the crack-tip in polycrystal by discrete dislocation dynamics. *Int J Solids Struct* 2019; 156–157:148–62. <https://doi.org/10.1016/j.ijssolstr.2018.08.012>.
- [45] Pande CS, Goswami R. Dislocation emission and crack dislocation interactions. *Metals (Basel)* 2020;10(4):1–14. <https://doi.org/10.3390/met10040473>.
- [46] Park CG, Lee CS, Chang YW. In situ TEM observations of crack tip dislocation behaviors under a mixed mode loading. In: *Mechanical behaviour of materials VI*; 1991. p. 3–9. <https://doi.org/10.1016/B978-0-08-037890-9.50395-1>.
- [47] Rice JR, Thomson R. Ductile versus brittle behaviour of crystals. *Philos Mag* 1974; 29(1):73–97. <https://doi.org/10.1080/14786437408213555>.
- [48] Wang TC. Fracture criteria for combined cleavage and dislocation emission. *Philos Mag A Phys Condensed Matter Struct Defects Mech Prop* 1996;74(4):983–1001. <https://doi.org/10.1080/01418619608242172>.
- [49] Goswami R. *Dislocation crack interactions and lattice rotation under uniaxial and cyclic loading*. Washington, DC: Naval Research Laboratory; 2018.
- [50] Rovinelli A, Lebensohn RA, Sangid MD. Influence of microstructure variability on short crack behavior through postulated micromechanical short crack driving force metrics. *Eng Fract Mech* 2015;138:265–88. <https://doi.org/10.1016/j.engfracmech.2015.03.001>.
- [51] Auld BA. *Acoustic fields and waves in solids volume i*. 1st ed. New York: Wiley; 1973.
- [52] Anderson TL. *Fracture mechanics - Fundamentals and applications*. CRC Press, Taylor & Francis Group; 1996.
- [53] Brown WF, Srawley JE. Plane strain crack toughness testing of high strength metallic materials. In: Committee E-24, editor. *Plane strain crack toughness testing of high strength metallic materials*. West Conshohocken, PA: ASTM International; 1966. p. 1–129. <https://doi.org/10.1520/STP44663S>.
- [54] Long DJ, Wan W, Dunne FPE. The influence of microstructure on short fatigue crack growth rates in Zircaloy-4: crystal plasticity modelling and experiment. *Int J Fatigue* 2022;107385. <https://doi.org/10.1016/j.ijfatigue.2022.107385>. Feb.
- [55] Joseph S, Bantounas I, Lindley TC, Dye D. Slip transfer and deformation structures resulting from the low cycle fatigue of near-alpha titanium alloy Ti-6242Si. *Int J Plast* 2018;100:90–103. <https://doi.org/10.1016/j.ijplas.2017.09.012>.
- [56] James LA. Environmentally aggravated fatigue cracking of Zircaloy-2. *Nucl Appl Technol* 1970;9(2):260–7. <https://doi.org/10.13182/nt70-a28815>.
- [57] Wisner SB, Reynolds MB, Adamson RB. Fatigue behaviour of irradiated and unirradiated Zircaloy and Zirconium. In: *Tenth international symposium on zirconium in the nuclear industry*; 1993. p. 499–520. Jun.
- [58] Logsdon WA, Liaw PK. Tensile, fracture toughness, and fatigue crack growth rate properties of zirconium copper. Springer-Verlag New York Inc; 1987.
- [59] Connolly M, et al. In situ high energy X-ray diffraction measurement of strain and dislocation density ahead of crack tips grown in hydrogen. *Acta Mater* 2019;180: 272–86. <https://doi.org/10.1016/j.actamat.2019.09.020>. Nov.
- [60] Y. Liu, W. Wan, S. El Chamaa, M.R. Wenman, C.M. Davies, and F.P.E. Dunne, “Creep and strain rate sensitivity in textured polycrystal Zr alloys (Submitted),” 2020.
- [61] J.J. Kearns, “Thermal expansion and preferred orientation in Zircaloy (LWBR development program),” United States, 1965. [Online]. Available: <https://www.osti.gov/biblio/6736579>.
- [62] Murakami Y. 4 - Effect of size and geometry of small defects on the fatigue limit. In: Murakami Y, editor. *Metal fatigue*. 2nd Ed. Academic Press; 2019. p. 39–59. <https://doi.org/10.1016/B978-0-12-813876-2.00004-2>.
- [63] Gong J, Benjamin Britton T, Cuddihy MA, Dunne FPE, Wilkinson AJ. (a) Prismatic, (a) basal, and (c+a) slip strengths of commercially pure Zr by micro-cantilever tests. *Acta Mater* 2015;96:249–57. <https://doi.org/10.1016/j.actamat.2015.06.020>.
- [64] Liu Y, Wan W, El Chamaa S, Wenman MR, Davies CM, Dunne FPE. Creep and strain rate sensitivity in textured polycrystal Zr alloys (In press). *Acta Mater* 2021 [Online]. Available, <https://arxiv.org/abs/2109.05333>.